The permeability of stylolite-bearing limestone

Michael Heap, Thierry Reuschlé, Patrick Baud, François Renard, Gianluca Iezzi

The permeability of stylolite-bearing limestone

Michael Heap[1], Thierry Reuschlé[1], Patrick Baud[1], François Renard[2,3], and Gianluca Iezzi[4]

[1]*Géophysique Expérimentale, Institut de Physique de Globe de Strasbourg (UMR 7516 CNRS, Université de Strasbourg/EOST), 5 rue René Descartes, 67084 Strasbourg cedex, France.*

[2]*PGP, The Njord Centre, Departments of Geosciences & Physics, University of Oslo, Norway*

[3]*Université Grenoble Alpes, Université Savoie Mont Blanc, CNRS, IRD, IFSTTAR, ISTerre, 38000 Grenoble, France*

[4]*Dipartimento di Ingegneria Geologia, IV Piano del Plz. Ex-Rettorato, Università degli Studi "G. d'Annunzio", Via Dei Vestini 30, 66100 Chieti, Italy.*

Corresponding author: M. Heap (heap@unistra.fr)

Abstract

Stylolites are planar features that form due to intergranular pressure solution. Due to their planar geometry and relative abundance in limestone reservoirs, their impact on regional fluid flow has attracted considerable interest. We present laboratory permeability data that show that stylolites can be considered as conduits for flow in the stylolite-bearing limestones measured. A combination of analysis techniques shows that this is due to a zone that surrounds these stylolites that is more porous and contains larger pores than the host rock. Our data also show that the water permeability of a sample containing a stylolite parallel to fluid flow is typically lower than its permeability to gas, explained here as a result of the expansion of minor amounts of clay found in the stylolite, and that, due to their microstructural similarities, tectonic and sedimentary stylolites affect sample permeability similarly. Finally, we show that the permeability anisotropy that

develops in the rock mass due to the presence of sedimentary stylolites makes it appear as though the stylolites are acting as barriers to fluid flow, and may explain the discrepancy between laboratory measurements and field-scale observations. This approach can provide estimates for the equivalent permeability, and permeability anisotropy, for stylolite-bearing limestone reservoirs worldwide.

Keywords: Stylolite; limestone; permeability; synchrotron X-ray computed tomography; scanning electron microscopy

Highlights

- Stylolites in limestones are conduits for flow, not barriers to flow.
- Stylolites are characterised by zone of higher porosity than the host rock.
- The high-porosity stylolite zone contains larger pores than in the host rock.
- Pores within stylolites are less spherical: stylolites create the high-porosity zone during their formation.
- Stylolites create a permeability anisotropy that may make them falsely appear as barriers to flow.

1 Introduction

Stylolites are planes of insoluble minerals that form in rocks as soluble minerals are removed by pressure solution (e.g., Park and Schot, 1968; Wanless, 1979; Nenna and Aydin, 2011; Croizé et al., 2013; Toussaint et al., 2018). They are common in limestones due to the relatively high solubility of calcite (e.g., Tondi et al., 2006; Fabricius and Borre, 2007; Benedicto and Schultz, 2010; Smith et al., 2011; Rustichelli et al., 2012; Agosta et al., 2012; Laronne Ben-Itzhak et al., 2014; Rustichelli et al., 2015; Martín-Martín et al., 2018), but are also found in sandstones (Heald, 1955; Walderhaug, 1996; Bjørkum et al., 1998; Walderhaug and Bjørkum, 2003; Emmanuel et al., 2010). Stylolites form perpendicular to the major compressive stress and are commonly found sub-parallel to bedding (formed by overburden stresses; "sedimentary stylolites"), but can form sub-perpendicular to bedding due to tectonic stresses ("tectonic stylolites"; e.g., Railsback and Andrews, 1995; Ebner et al., 2010a). Although macroscopically planar, stylolites are morphologically variable on the meso- and microscale (e.g., Karcz and Scholz, 2003; Renard et al., 2004; Schmittbuhl et al., 2004; Rolland et al., 2012; Laronne Ben-Itzhak et al., 2012; Rolland et al., 2014; Koehn et al., 2016). Their roughness is thought to be a function of the magnitude of the stress under which they formed (e.g., Koehn et al., 2007; Ebner et al., 2009a; Koehn et al., 2012), the heterogeneity of the host material (e.g., Andrews and Railsback, 1997; Brouste et al., 2007; Ebner et al., 2009b, 2010b; Koehn et al., 2012), and/or the competition between long-range elastic redistribution and surface tension forces along the interface (e.g., Schmittbuhl et al., 2004; Renard et al., 2004).

Due to their macroscopically planar form, the influence of stylolites on fluid flow and reservoir compartmentalisation has drawn considerable interest. A handful of experimental studies have shown that stylolites can provide conduits for flow (Lind et al., 1994; Mallon and Swarbrick, 1998; Heap et al., 2014; Rustichelli et al., 2015), challenging paradigms that stylolites present barriers to fluid flow (Dunnington, 1967; Nelson, 1981; Burgess and Peter, 1985; Koepnick, 1987; Finkel and Wilkinson, 1990; Dutton and Willis, 1998; Alsharhan and Sadd, 2000). Heap et al.

(2014), for example, measured the permeability of limestone samples that contained no stylolites, one stylolite perpendicular to the imposed fluid flow, or one stylolite parallel to flow. They found that samples containing stylolites parallel to flow were about an order of magnitude more permeable than the stylolite-free material. They concluded that this was likely due to a zone of enhanced porosity surrounding the stylolite, a conclusion supported by microstructural observations (Carozzi and von Bergen, 1987; Raynaud and Carrio-Schaffhauser, 1992; van Geet et al., 2000; Gringas et al., 2002; Padmanabhan et al., 2015). The higher porosity zone surrounding a stylolite has also been shown to reduce the uniaxial compressive strength of a stylolite-bearing sample (Baud et al., 2016). However, although stylolites themselves may act as conduits for fluid flow (e.g., Heap et al., 2014; Rustichelli et al., 2015), we highlight that they are the by-product of a process whereby dissolved materials are often precipitated into the pore space of the adjacent rock, thereby lowering the porosity, and presumably permeability, relative to the original host rock (see Toussaint et al. (2018) for a review). Therefore, formations containing abundant stylolites will likely be characterised by lower porosities and permeabilities than neighbouring stylolite-free formations. Indeed, stylolite density has been measured to be inversely proportional to porosity in some limestone formations (e.g., Alsharhan and Sadd, 2000).

We extend the study of Heap et al. (2014) by providing new porosity-permeability data for stylolite-bearing limestones. We also (1) compare the gas and water permeability of stylolite-bearing limestones and (2) compare the permeabilities of limestone samples containing sedimentary and tectonic stylolites. Our experimental data are supported by microstructural observations (scanning electron microscope, SEM), multi-resolution (voxel size of 6.27 and 0.7 μm) synchrotron X-ray computed tomography (CT), and estimations of the average pore radius of the flow path used by gas particles determined using the Klinkenberg slip factor. Finally, and using our experimental data, we consider the "upscaled" permeability of a limestone rock mass containing stylolites.

2 Experimental materials and methods

We selected six stylolite-bearing limestones for this study: two from open quarries in Burgundy (France) (Corton limestone and Comblanchien limestone, both Jurassic) and four from cores drilled around the ANDRA Underground Research Laboratory near Bure (France) (one from the Middle Jurassic "Dogger" series and three from the Late Jurassic Oxfordian stage). The porosities and gas permeabilities of some of the samples from Bure were previously presented in Heap et al. (2014). We provide here new water permeability data on these samples and new porosity and permeability (gas and water) data for additional samples taken from one of the cores from Bure (from the Late Jurassic Oxfordian stage) and the samples from Burgundy.

We first quantified the mineral content of our experimental materials using X-ray powder diffraction (XRPD). Powdered samples of each of the limestones were ground for 10 minutes in alcohol using an agate pestle and mortar. The XRPD analyses were performed on powdered mounts (using nominally zero-background Si sample holders and 10-20 mg of material) using a Bruker D-5005 θ-2θ Bragg-Brentano diffractometer equipped with Ni-filtered CuKα radiation. The obtained XRPD patterns were first checked for their crystalline content using search-match comparisons with XRPD standards contained in the inorganic crystal structure database (ICSD). The XRPD patterns with more than one crystalline phase were then refined using the software EXPGUI-GSAS (Larson and Von Dreele 1994; Toby 2001). EXPGUI-GSAS uses the Rietveld method to derive crystallographic parameters and phase abundances (wt. %). More detailed descriptions of the Rietveld refinement method are reported in Iezzi et al. (2004; 2010 and references therein). XRPD analysis was performed on (1) stylolite-free material and (2) on samples cut to contain a stylolite, but with as little host rock as possible (in an attempt to identify the minerals forming the stylolite). In addition, minerals within the stylolites were also identified using energy-dispersive X-ray

117 spectroscopy (EDS) during our SEM analyses. The mineral content for the Bure samples was
118 previously presented in Heap et al. (2014).

119 The first of the Oxfordian limestones (O1; depth = 159 m) is a heterogeneous allochemical
120 limestone that contains ooids, peloids, shell fragments, and fossil foraminifera within a micrite
121 matrix (Figure 1a). The ooids are typically 0.1-0.25 mm in diameter (Figure 1a). The peloids are
122 noticeably larger than the ooids (Figure 1a); some peloids have diameters greater than 1 mm. Shell
123 fragments in O1 can be many millimetres in length. O1 is predominately calcite (99 wt. %) with
124 subordinate dolomite (<1 wt. %) (Table 1). The second Oxfordian limestone (O3; depth = 174 m) is
125 a well-sorted allochemical limestone that contains ooids, typically 0.25-0.5 mm in diameter, within
126 a micrite matrix (Figure 1b). O3 is predominately calcite (99 wt. %) with subordinate dolomite (<1
127 wt. %), gypsum (<1 wt. %), and pyrite (<<1 wt. %) (Table 1). The third Oxfordian limestone (O6;
128 depth = 364 m) is a very heterogeneous allochemical limestone that contains peloids, shell
129 fragments (>1 mm), and fossil foraminifera (>1 mm) within a micrite matrix (Figure 1c). O6 is
130 predominately calcite (99 wt. %) with subordinate dolomite (<1 wt. %) and pyrite (<<1 wt. %)
131 (Table 1). The "Dogger" limestone (D3; depth 747 m) is an orthochemical limestone (micrite)
132 (Figure 1d) composed of 93 wt. % calcite, 4 wt. % dolomite, 3 wt. % quartz, and subordinate pyrite
133 (<<1 wt. %) (Table 1). Corton limestone is an allochemical limestone that contains peloids
134 (typically 0.2-1 mm in diameter) within a micrite matrix (Figure 1e). Corton limestone is
135 predominately calcite (99 wt. %) with subordinate quartz (<1 wt. %) (Table 1). Comblanchien
136 limestone is a heterogeneous allochemical limestone that contains ooids, peloids, shell fragments,
137 and fossil foraminifera within a micrite matrix (Figure 1f). Allochems are typically between 0.1 and
138 1 mm in diameter (Figure 1f). Comblanchien limestone is essentially entirely calcite in composition
139 (99 wt. %) (Table 1).

140 Examples of the stylolites in these materials are shown in Figures 2, 3, 4, and 5.
141 Qualitatively, there are clear differences between the sedimentary stylolites in terms of thickness

and roughness/tortuosity (Figures 2, 3, and 4). The thickest stylolites (up to 2-3 mm) are found in the D3 samples (Figure 3a). The stylolites in Corton limestone are the most rough/tortuous (Figure 4a); the least rough/tortuous stylolites are found in samples O3 (Figure 2b) and the Comblanchien limestone (Figure 4b). Stylolites found in the most heterogeneous limestone—sample 06—are correspondingly anastomosing (Figure 2c). We also provide images of tectonic and sedimentary stylolites found in sample O3 (Figure 5). There are no discernable differences between the thickness and roughness/tortuosity between the tectonic and sedimentary stylolites in sample O3 (Figure 5). A combination of XRPD and EDS analyses found that the stylolites typically consist of dolomite and/or quartz, with minor quantities of pyrite and organic matter/clay (Table 1).

Cylindrical samples (20 mm in diameter and nominally 40 mm in length) were cored from the blocks/cores. Samples were prepared to contain (1) one stylolite perpendicular to the axis of the core (i.e. perpendicular to the imposed flow direction), (2) one stylolite parallel to the axis of the core (i.e. parallel to the imposed flow direction), or (3) no stylolite (where possible, stylolite-free samples were prepared in two or three orthogonal directions). The samples containing no stylolites were typically prepared from material 5-10 cm from the stylolite studied. We also prepared samples containing tectonic stylolites either perpendicular or parallel to the core axis from one of the Oxfordian limestones (sample O3). We note that, following sample preparation, our samples did not contain any obvious stylolite-associated fractures. Representative photographs of the 20 mm-diameter samples prepared for laboratory testing (stylolite-free, one stylolite perpendicular to the sample axis, and one stylolite parallel to the sample axis) are provided in Figures 6 and 7. Figure 8 shows photographs of samples of O3 containing tectonic and sedimentary stylolites.

The connected porosity of each sample was determined using the triple weight water saturation technique (Guéguen and Palciauskas, 1994). Gas (argon or nitrogen) and water (distilled water) permeabilities were then measured in a hydrostatic pressure vessel under a confining

pressure of 2 MPa. All measurements of water permeability were performed using the steady-state flow method. Following microstructural equilibrium, a pressure differential was imposed across the sample and the flow rate was measured using an electronic balance (with a precision ± 0.0005 g). Once steady-state flow had been established, the water permeability k_{water} was determined using Darcy's relation:

$$\frac{Q}{A} = \frac{k_{water}}{\eta L}\left(P_{up} - P_{down}\right), \quad (1)$$

where Q is the volumetric flow rate, A is the cross-sectional area of the sample, P_{up} and P_{down} represent the upstream and downstream pressure, respectively (where P_{down} is the atmospheric pressure), L is the length of the sample, k_{water} is the permeability to water, and η is the viscosity of the pore fluid (taken here as 1.008×10^{-3} Pa s). A pressure differential (i.e. $P_{up} - P_{down}$) of 0.5 MPa was used for all measurements reported herein.

Gas (argon or nitrogen) permeability was measured using either the steady-state method (for high-permeability samples) or the pulse-decay method (for low-permeability samples). For the steady-state method, a pressure differential was imposed across the sample (following microstructural equilibrium) and the outlet flow rate was measured using a flow meter. Since the pore fluid is compressible, the raw permeability to gas k_{gas_raw} is expressed as (Scheidegger, 1974):

$$\frac{Q}{A} = \frac{k_{gas\_raw}}{\eta L}\frac{(P_{up})^2 - (P_{down})^2}{2P_{down}}, \quad (2)$$

where η, the viscosity of the pore fluid, was taken as 2.21×10^{-5} and 1.78×10^{-5} Pa s for argon and nitrogen, respectively. Steady-state volumetric flow rate Q measurements were taken under several

pore pressure differentials (i.e. $P_{up} - P_{down}$, where P_{down} is the atmospheric pressure) to check whether any auxiliary corrections were required. We first plot $1/k_{gas\_raw}$ as a function of Q to check whether the Forchheimer correction is required (Forchheimer, 1901). The correction is necessary if these data can be well described by a linear fit with a positive slope. The Forchheimer-corrected permeability is taken as the inverse of the y-intercept of the best-fit linear regression in the plot of $1/k_{gas\_raw}$ as a function of Q. If the Forchheimer correction is not required, we then check whether the Klinkenberg correction is required (Klinkenberg, 1941). To do so, we plot k_{gas_raw} as a function of the reciprocal mean pressure $1/P_m$, where P_m is the mean pore fluid pressure (i.e. $(P_{up} + P_{down})/2$). The Klinkenberg correction is required if these data can be well described by a linear fit with a positive slope and, if true, the Klinkenberg-corrected permeability can be taken as the y-intercept of the best-fit linear regression in the plot of k_{gas_raw} as a function of $1/P_m$. The Klinkenberg correction was required for all samples measured using the steady-state method; the Forchheimer correction was not required.

We used the pulse-decay method (Brace et al., 1968) to measure the gas permeability of the low-permeability samples. Following microstructural equilibrium at the target confining pressure, the decay of an initial pore pressure differential ($P_{up} - P_{down}$ = 0.5 MPa, where P_{down} is the atmospheric pressure) was monitored using a pressure transducer following the closure of the upstream pressure inlet. The gas permeability k_{gas_raw} was then determined using the following relation:

$$k_{gas\_raw} = 2\frac{\eta L}{A}\frac{V_{up}}{{P_{up}}^2 - {P_{down}}^2}\frac{dP_{up}}{dt}, \quad (3)$$

where V_{up} is the volume of the upstream pore pressure circuit (7.8×10^{-6} m^3) and t is time. As before, we checked whether these data required any auxiliary corrections (the Forchheimer or

212 Klinkenberg correction). The Klinkenberg correction was required for all samples measured using
213 the pulse-decay method; the Forchheimer correction was not required. A detailed description of
214 these permeability methods is available in Heap et al. (2017).
215
216 **3 Results**
217 The gas permeability data for the stylolite-free limestones as a function of connected
218 porosity are shown in Figure 9a. The data of Lind et al. (1994), a study that also measured the
219 permeability of stylolite-bearing carbonate rocks, are also included on Figure 9 because they
220 preserve a higher porosity (porosity > 0.2) than the samples measured herein. Our data show that
221 gas permeability increases as connected porosity is increased, in accordance with previously
222 published studies on the permeability of limestones (e.g., Ehrenberg et al., 2006; Zinszner and
223 Pellerin, 2007), and that there is no measurable permeability anisotropy in the studied materials
224 (Figure 9a contains data on samples cored in orthogonal directions, see Table 2). The difference
225 between permeability to gas and permeability to water in the stylolite-free samples appears to
226 depend on the connected porosity: permeability to gas can be a factor of 4.5 higher at low porosity
227 (porosity < 0.05) and the ratio between gas and water permeability is essentially unity at the
228 highest tested porosity (porosity ~0.15) (Figure 10a).
229 The porosity-permeability data for the stylolite-free and stylolite-bearing (perpendicular
230 and parallel to flow) limestones are shown in Figure 9b, together with the high-porosity (porosity >
231 0.2) data of Lind et al. (1994). Our data show that (1) the permeabilities of the samples containing
232 stylolites perpendicular to the direction of flow are similar to those of the stylolite-free samples and
233 (2) the permeabilities of the samples containing stylolites parallel to the direction of flow are
234 characterised by permeabilities higher than those of the stylolite-free samples (Figure 9b). In detail,
235 we notice that larger differences between the permeability of the samples containing stylolites
236 parallel to the direction of flow and the stylolite-free samples are observed at lower connected

porosities (Figure 9b). For example, the permeability of stylolite-bearing Corton limestone (porosity ~0.03) can be two or three orders of magnitude higher than the stylolite-free material (Figure 9b). The ratio of gas to water permeability for all the samples tested (including stylolite-free samples and samples containing stylolites perpendicular and parallel to flow) is plotted as a function of connected porosity in Figure 10b. As for the stylolite-free limestones (Figure 10a), high-porosity (porosity ~0.15) samples containing stylolites show little difference between gas and water permeability (Figure 10b). The gas permeabilities of the low-porosity samples containing stylolites are higher than their water permeabilities; this is especially true for the low-porosity samples containing stylolites parallel to flow (the difference for one sample is more than an order of magnitude) (Figure 10b).

Our data also show that there is essentially no difference between the influence of sedimentary and tectonic stylolites on the permeability of our limestone samples (Figures 9b and 10b; Table 2).

4 Discussion

4.1 Barriers to or conduits for fluid flow?

Our new permeability data are in agreement with the conclusion of Heap et al. (2014) and Rustichelli et al. (2015): the stylolites measured are not barriers to flow, but conduits for flow (Figure 9b). Heap et al. (2014) postulated that a zone of higher porosity surrounds a stylolite and that it is this high-porosity zone that enhances the circulation of fluids, as suggested by Carozzi and von Bergen (1987), Raynaud and Carrio-Schaffhauser (1992), and Van Geet et al. (2000). The greater increase in permeability in the low-porosity samples (when comparing the permeability of a stylolite-free sample to a sample containing a stylolite parallel to flow) (Figure 9b) is likely a consequence of their low matrix permeabilities. Conduits for flow have a much greater impact on

262 the equivalent permeability of low-porosity samples than on high-porosity samples, since the
263 matrix permeability of a high-porosity sample is much closer to the permeability of the fracture (as
264 observed in variably porous fractured materials; e.g., Heap and Kennedy, 2016; Kushnir et al.,
265 2018).

266 To image the hypothesised zone of higher porosity, we first provide a backscattered
267 scanning electron microscope (BSE) image of a stylolite within sample D3, selected due to its low
268 matrix porosity and permeability. This image shows that the matrix-stylolite interface is populated
269 by numerous micropores, typically only a few microns in diameter (white arrows; Figure 11). To
270 better resolve the porosity, and distribution of porosity, around a stylolite, we also provide multi-
271 resolution (voxel size of 6.27 (beamline MB05) and 0.7 μm (beamline ID19) and energy of 35 keV)
272 three-dimensional X-ray tomography imaging performed on a stylolite within sample D3 at the
273 European Synchrotron Radiation Facility (Grenoble, France). Because of the high-contrast between
274 the porosity and the minerals that comprise the rock (primarily calcite, quartz, and dolomite; Table
275 1), it is straightforward to segment the porosity so that individual pores can be imaged (Figure 12).
276 The segmented images show that the stylolite is associated with a zone of high porosity (Figure 12),
277 as previously measured by Baud et al. (2016). In particular, we observe that (1) the pores
278 surrounding the stylolite are larger than those within the host rock (Figure 12) and (2) some of the
279 pores are aligned with the teeth of the stylolite and are characterised by a "finger-like" shape
280 (Figure 13). Indeed, analysing the X-ray tomography data (similar to X-ray tomographic analyses
281 performed on intact porous limestones by Ji et al., 2012; 2014) show that the pores are larger
282 inside the stylolite (Figure 14a) and that the pores within the stylolite are characterised by lower
283 values of sphericity (where 1.0 is a perfect sphere; sphericity is defined using the Thermo Scientific
284 Avizo toolbox as $(\frac{1}{Shape_{VA3D}})^{1/3}$ where $Shape_{VA3D} = Area_{3D}{}^3/(36 \times \pi \times Volume_{3D}{}^2)$) (Figure 14b).
285 The volume of an individual pore within the stylolite varies from a few μm^3 up to $>10^5$ μm^3; the
286 volume of the pores outside the stylolite are all $<10^4$ μm^3 (Figure 14a). The average equivalent

diameter of the pores inside and outside the stylolite is 36.5 μm (standard deviation of 26.8 μm) and 11.1 μm (standard deviation of 4.7 μm), respectively. Sphericity inside and outside the stylolite varies from 0.2 to 0.4 and 0.4 and 0.9, respectively (Figure 14b). Since the shape of the pores are sometimes linked to the shape of the stylolite (Figure 13), we additionally conclude that such porosity is likely the consequence of stylolite formation (in agreement with the conclusions of Raynaud and Carrio-Schaffhauser (1992) and Carozzi and von Bergen (1987)), rather than that stylolites form preferentially in a zone of higher porosity (as hypothesised by Braithwaite, 1989).

To complement these microstructural data, we use the Klinkenberg slip factor, b (which has the units of pressure; Table 2) (Klinkenberg, 1941), to provide an independent assessment of the average pore radius used by the gas molecules. Since the pore radius determined using this technique uses data from permeability experiments, it will therefore yield the average pore throat radius (in contrast to the CT data, which provides information on the pores). Since the mean free path is inversely proportional to P_m, Poiseuille's law for gas flow in a cylindrical tube and Darcy's law for flow in porous media yields the following relation:

$$k_{gas} = k_{gas\_raw}\left(1 + \frac{b}{P_m}\right), \quad (4)$$

where k_{gas} is the true (i.e. Klinkenberg-corrected) gas permeability (Klinkenberg, 1941). The average pore throat radius of the flow path followed by the gas molecules, r, can be estimated using the following relation (Civan, 2010):

$$r = \frac{4}{b}\eta\sqrt{\frac{\pi R_g T}{2M_w}}, \quad (5)$$

where R_g is the ideal gas constant (taken as 8.31 J mol^{-1} K^{-1}), T is the temperature (taken as 293 K), and M_w is the molar mass of the pore fluid (taken as 0.03995 and 0.02802 kg mol^{-1} for argon and nitrogen, respectively). The Klinkenberg slip factor has previously been used to examine the average pore throat radius of the flow path in rocks such as shales (e.g., Heller et al., 2014; Firouzi et al., 2014; Letham and Bustin, 2016) and, more recently, volcanic rocks (Heap et al., 2018) using the same, or similar, method (i.e. Equation (5)). We find that the average pore throat radius of the flow path followed by the gas molecules in the stylolite-free samples, excluding the Corton limestone samples, varies between ~0.05 and 0.15 μm (Figure 15a). Excluding Corton limestone, the samples containing the highest porosities (porosity ~0.15) are characterised by the largest pore throat radii (~0.1 to ~0.15 μm; Figure 15a). The average pore throat radius of the flow path followed by the gas molecules is much larger in Corton limestone, varying between ~0.2 and 0.35 μm (Figure 15a). Although not obvious from our microstructural observations (Figure 1e), Corton limestone must contain larger pore throats than the other limestones measured herein. The average pore throat radii of the flow paths followed by the gas molecules in the samples containing stylolites (together with the stylolite-free samples) are provided in Figure 15b. The data show that (1) the pore throat radii forming the flow path in the samples containing stylolites perpendicular to flow are similar to the stylolite-free samples and (2) the pore throat radii along the flow path parallel to the stylolite are systematically larger than those of the other samples (Figure 15b). These data suggest that the stylolites are associated with pore throats with larger radii than those that typify the host rock. This conclusion is in agreement with our X-ray tomography analysis, which shows that the pores are larger inside the stylolite than in the host rock (Figure 14a). As expected, the radii predicted using Equation (5) are much smaller (typically < 1 μm; Figure 15) than the range of radii predicted from the X-ray tomography analysis (up to a few tens of microns). This is because the Klinkenberg analysis (Equation 5) yields the pore throat radius and the X-ray tomography analysis yields the pore radius.

We conclude here that stylolites present conduits for, rather than barriers to, flow (Figure 9b) in limestones measured herein. This can be explained by a zone of elevated porosity (Figure 12) that contains pores and pore throats with larger radii than the host rock (Figures 14a and 15a), which we conclude must develop around a stylolite during its formation. The development of stylolitic porosity is discussed in detail in Carozzi and von Bergen (1987) and is considered the result of grainscale heterogeneities in the rock during the dissolution process.

4.2 Differences between tectonic and sedimentary stylolites

Our permeability data suggest, for the materials studied herein, that there is essentially no difference between the influence of sedimentary and tectonic stylolites on the permeability of a stylolite-bearing sample: both sedimentary and tectonic stylolites are conduits for fluid flow (Figure 9b; Table 2). This is perhaps not surprising since they are very similar on the microscale (Figure 5) and on the sample lengthscale (Figure 8). The fact that tectonic stylolites are also conduits for flow (Table 2) further supports the hypothesis that stylolites create a zone of higher porosity during their formation (e.g., Raynaud and Carrio-Schaffhauser, 1992; Carozzi and von Bergen, 1987), rather than that they form preferentially in higher porosity layers (e.g., Braithwaite, 1989).

4.3 Differences between gas and water permeability

Differences between permeability to gas and water are typically observed in the presence of swelling clays (e.g., Faulkner and Rutter, 2000, 2003; Tanikawa and Shimamoto 2006; Davy et al., 2007; Tanikawa and Shimamoto 2009; Behnsen and Faulkner, 2011). Our XRPD analyses highlight that clays are below the detection limit in the stylolite-free material (Table 1). It is therefore perhaps surprising that we see about a fourfold difference between gas and water permeability in the low-porosity limestones (Figure 10a). A recent study found that the permeability to gas was

higher than permeability to water in two volcanic rocks (basalt and andesite) by a factor of up to five (Heap et al., 2018). In the absence of significant physicochemical reactions, these authors suggested that the difference in gas and water permeabilities is likely due to water adsorption on the surface of thin microstructural elements. For the stylolite-free limestones, we find that there is essentially no difference between the gas and water permeabilities for the samples characterised by the largest average pore throat radii (~0.1 to ~0.15 μm) (Table 2), as determined using the Klinkenberg slip factor. Samples with average pore throat radii between ~0.05 and 0.1 μm are more permeable to gas than to water (Table 2). Similar to the conclusions drawn by Heap et al. (2018), we conclude here that, in the absence of clay within the intact materials (Table 1), the difference in gas and water permeabilities is likely due to water adsorption on the surface of thin (~0.05 to 0.1 μm) microstructural elements.

Measurements of gas and water permeability on the samples containing stylolites show that samples containing stylolites parallel to flow are often more permeable to gas than water, by up to one order of magnitude (Figure 10b). Since average pore throat radius of the flow path followed by the gas molecules is relatively high for these samples (up to ~1 μm; Figure 15b), we conclude that the difference in gas and water permeabilities in these samples are due to minor quantities of clay found within the stylolite (identified by EDS during our SEM analyses; Table 1). The expansion of clay minerals in contact with water constricts pore throats and thus reduces permeability (e.g., Faulkner and Rutter, 2003).

4.4 Implications for fluid flow in limestone reservoirs

Limestone forms an important component of the Earth's continental crust (Ehrenberg et al., 2006; Ford and Williams, 2013) and, as a result, the permeability of limestone reservoirs is not only important for fluid flow and pore pressure distribution within the crust, but also for the exploitation of hydrocarbon reserves.

Our study shows that stylolites in limestone present conduits for flow (Figure 9b) due to a zone of elevated porosity, containing pores with larger radii than the host rock, which develops around a stylolite during its formation (Figures 11, 12, 14, and 15). In order to consider fluid flow in stylolite-bearing limestone reservoirs, we must first upscale our laboratory measurements. One method to upscale such laboratory data is to first extract the permeability of a stylolite. The permeability of a stylolite, k_{stylo}, can be determined using a two-dimensional model that considers flow in parallel layers (the same model used to determine the permeability of compaction bands in Vajdova et al. (2004) and fractures in Heap and Kennedy (2016), Farquharson et al. (2016), and Kushnir et al. (2018)):

$$k_{stylo} = \frac{(A \cdot k_e) - (A_{intact} \cdot k_0)}{A_{stylo}} \quad (6)$$

where A is the cross-sectional area of the sample, k_e is the equivalent permeability (the permeability of the stylolite-bearing sample), A_{intact} is the area of stylolite-free material, k_0 is the stylolite-free permeability, and A_{stylo} is the area of the stylolite. For the purpose of this exercise, we will consider a core of Dogger limestone (D3) taken from the ANDRA Underground Research Laboratory at Bure (Figure 16). To calculate k_{stylo} we use the permeability of the stylolite-free sample of D3 (k_0 = 3.69 × 10^{-19} m^2; Table 2). The equivalent permeability, k_e, is permeability of the D3 sample containing a stylolite parallel to the direction of flow (k_e = 5.98 × 10^{-18} m^2; Table 2), and we use a stylolite thickness of 1 mm (a reasonable approximation of the thickness of the stylolite in this sample; Figure 6d). Using these values, Equation (6) yields a stylolite permeability, k_{stylo}, of 8.85 × 10^{-17} m^2. We can now model the equivalent permeability of a rock mass populated with stylolites using our value for k_{stylo} and the following relation:

$$k_e = \frac{(w_{intact} \cdot k_0) + (w_{stylo} \cdot k_{stylo})}{W}, \quad (7)$$

where w_{intact} is the total width of the intact material, w_{stylo} is the total width of the stylolites, and W is the length of rock considered ($W = w_{intact} + w_{stylo}$). The Dogger limestone core sample shows that there are five sedimentary stylolites over a length of about 25 cm (i.e. a stylolite density of 20 m^{-1}) (Figure 16). Although stylolite thickness varies (Figure 16) we will, for simplicity, assume that the thickness of each stylolite is 1 mm. Therefore, according to our model (Equation (7); W = 250 mm; w_{stylo} = 5 mm; w_{intact} = 245 mm; k_0 = 3.69 × 10^{-19} m^2; k_{stylo} = 8.85 × 10^{-17} m^2), the equivalent permeability parallel and perpendicular to bedding for the limestone core shown in Figure 16 is 1.80 × 10^{-17} and 3.69 × 10^{-19} m^2, respectively. In other words, the 25 cm-long sample is 50 times more permeable parallel to bedding than perpendicular to bedding. Therefore, although stylolites are conduits for flow, they can create a permeability anisotropy in a rock unit or reservoir that may make it appear that they form barriers to fluid flow (because permeability perpendicular to bedding is lower than the permeability parallel to bedding) and may therefore explain the discrepancy between laboratory measurements (that suggest that stylolites are conduits) and field-scale investigations (that suggest that stylolites are barriers). It is important to highlight that these equivalent permeability estimates for a stylolite-bearing rock mass are just one snapshot in the porosity-permeability evolution of this limestone formation. For example, it is likely that, prior to pressure-solution and the formation of the stylolites, the host rock was much more porous and more permeable. Although not considered in our simple model, we note that the presence of stylolites perpendicular to bedding (i.e. tectonic stylolites) will reduce such permeability anisotropy. Indeed, if the number of tectonic stylolites equals the number of sedimentary stylolites, no permeability anisotropy will be observed. Although tectonic stylolites are not uncommon in limestone reservoirs (Railsback and Andrews, 1995; Ebner et al., 2010a; Figure 8), it is difficult to

assess their density at the ANDRA Underground Research Laboratory at Bure due to the drilling direction (perpendicular to bedding). The simple method presented above can be easily adapted to provide estimates for the equivalent permeability, and permeability anisotropy, for stylolite-bearing (both sedimentary and tectonic) limestone reservoirs worldwide.

Although we conclude here that our stylolites form conduits for fluid flow, we cannot rule out that some stylolites, different to those measured here, may provide barriers to flow. For example, (1) stylolites may provide barriers to flow if they are characterised by thick and continuous layers of clay-rich material, (2) an abstract by Corwin et al. (1997) suggests that stylolites associated with a cemented zone could be of lower permeability than the surrounding host rock, and (3) the modelling of Koehn et al. (2016) suggests that stylolites with simple geometries (e.g., "simple wave-like type") may be more likely to provide barriers to flow. We also highlight that, due to differences in mineral composition and microstructure, the influence of stylolites on the permeability of sandstone may differ from their influence on the permeability of carbonate rocks (e.g., Walderhaug and Bjørkum, 2003; Emmanuel et al., 2010).

Therefore, and although we provide laboratory measurements for the permeability of stylolite-bearing limestone from six formations collected from two locations within France, more laboratory measurements on stylolites that are characterised by thick and continuous layers of clay-rich material are now required to further explore the role of stylolites on the regional-scale permeability of limestone reservoirs (as concluded by Bruna et al., 2018). Laboratory measurements on stylolite-bearing sandstones also offer an interesting avenue for future research.

5 Conclusions

The salient conclusions of this study can be summarised thusly:

(1) The stylolites measured herein are conduits for fluid flow, not barriers to fluid flow.

(2) The permeability of a stylolite-bearing sample is lower when measured with water than with gas. We interpret this here as the result of the expansion of minor quantities of clay found within the stylolite. The expansion of clay minerals constricts pore throats and thus reduces permeability.

(3) Sedimentary and tectonic stylolites affect sample permeability similarly. We interpret this as a result of their similar microstructures.

(4) X-ray tomography data show that the stylolites are surrounded by a zone of higher porosity that is characterised by pores larger than those found in the intact material. This explains why the stylolites measured herein are conduits for fluid flow.

(5) The presence of larger pores within the stylolite zone is supported by an analysis of the Klinkenberg slip factor, which highlights that the average pore throat radius of the flow path followed is larger when the sample contains a stylolite parallel to flow.

(6) X-ray tomography data show that the pores within the stylolite are much less spherical than those of the host rock and that they are sometimes aligned with the teeth of the stylolite. Since the shape of the pores are linked to the shape of the stylolite, we conclude that such porosity is likely the consequence of stylolite formation, rather than that stylolites form preferentially in a zone of higher porosity.

(7) Upscaling our laboratory measurements using a simple two-dimensional model that considers flow in parallel layers shows that the equivalent permeability of a stylolite-bearing limestone rock mass is higher parallel to bedding than perpendicular to bedding.

(8) The permeability anisotropy that develops in the rock mass due to the presence of stylolites makes it appear as though the stylolites are acting as barriers to fluid flow (since permeability perpendicular to bedding is lower than the permeability parallel to bedding) and may explain the discrepancy between laboratory measurements and field-scale observations.

Acknowledgements

This research was partly funded by CNRS and ANDRA (FORPRO program) and the Norwegian Research Council (project ARGUS, grant 272217). We would like to thank Alexandra Rolland, Silvio Mollo, Gilles Morvan, and Bertrand Renaudié. We thank Gilles Jouillerot (Rocamat Pierre Naturelle) for his help selecting the materials at Comblanchien and Elodie Boller for her help at the European Synchrotron Radiation Facility (beamline ID19). The comments of Einat Aharonov and one anonymous reviewer helped improve this manuscript.

Data availability

Most of the data used in this study are available in Tables 1 and 2. The X-ray tomography data may be made available on request (to François Renard).

490 **Figure captions**

491

492 **Figure 1**. Optical microscope images of the stylolite-free (host rock) material for the studied
493 limestones. (a) Sample O1 – Oxfordian limestone from Bure. (b) Sample O3 – Oxfordian limestone
494 from Bure. (c) Sample O6 – Oxfordian limestone from Bure. (d) Sample D3 – "Dogger" limestone
495 from Bure. (e) Corton limestone from Burgundy. (f) Comblanchien limestone from Burgundy.

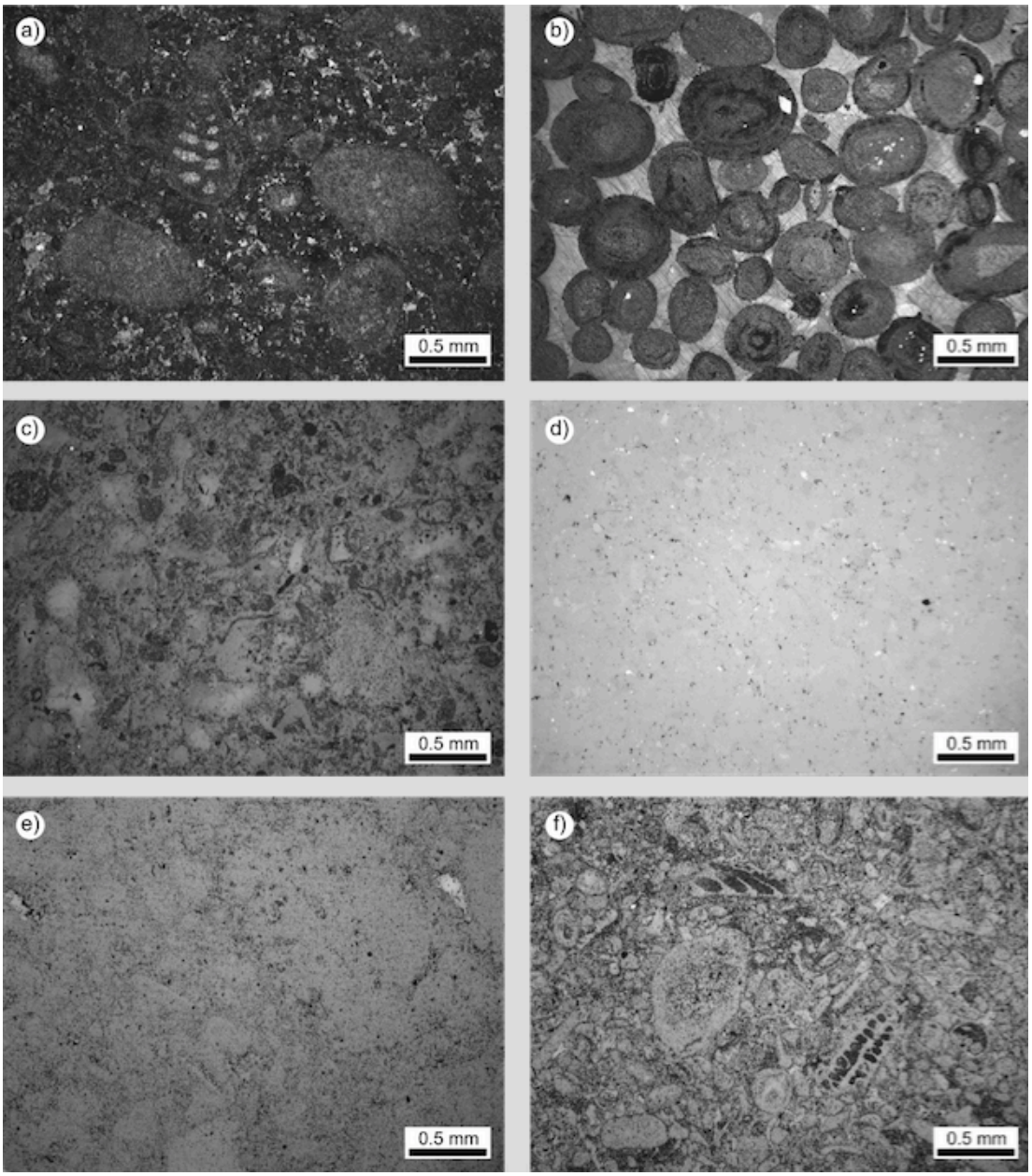

496

Figure 2. Optical microscope images of the stylolites found within studied limestones. (a) Sample O1 – Oxfordian limestone from Bure. (b) Sample O3 – Oxfordian limestone from Bure. (c) Sample O6 – Oxfordian limestone from Bure.

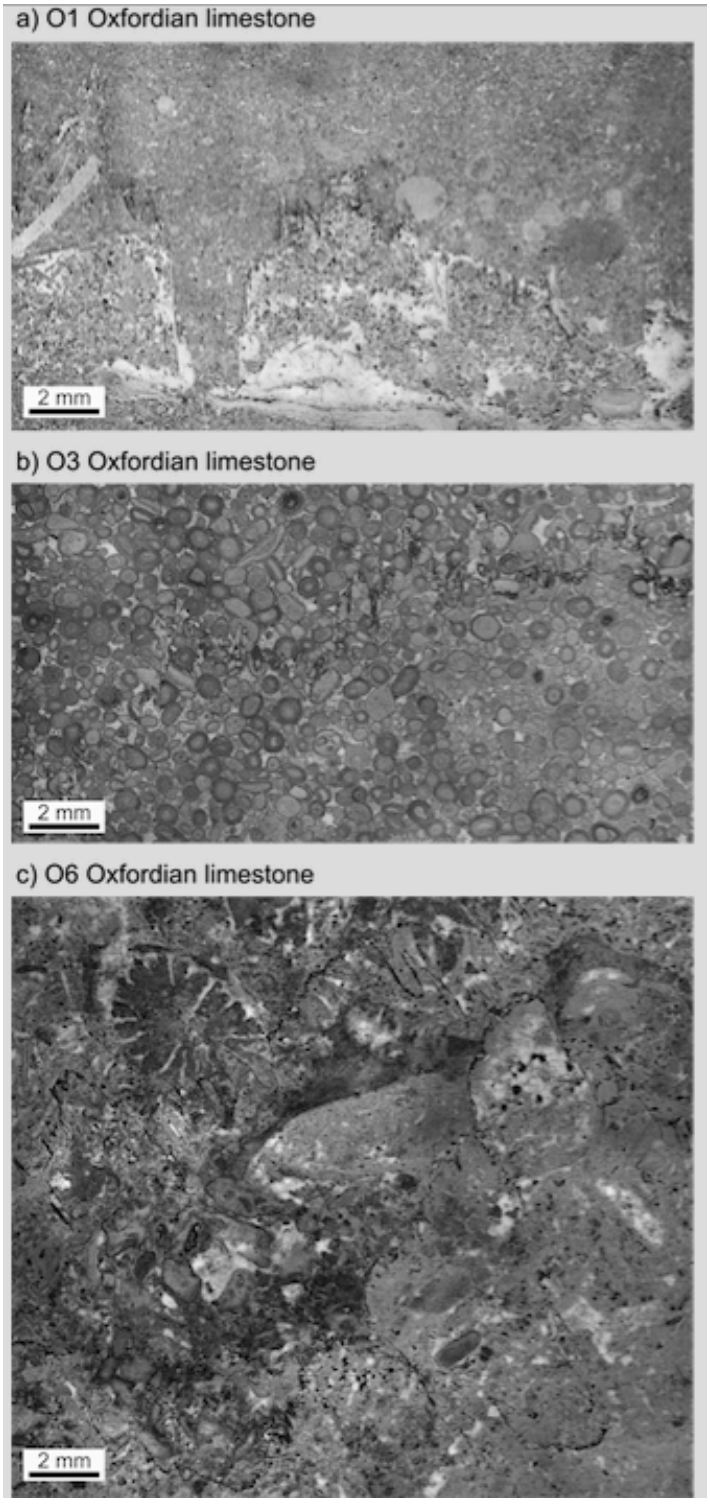

501 **Figure 3**. Optical microscope images of the stylolites found within studied limestones. (a) Sample

502 O6 – Oxfordian limestone from Bure. (b) Sample D3 – "Dogger" limestone from Bure.

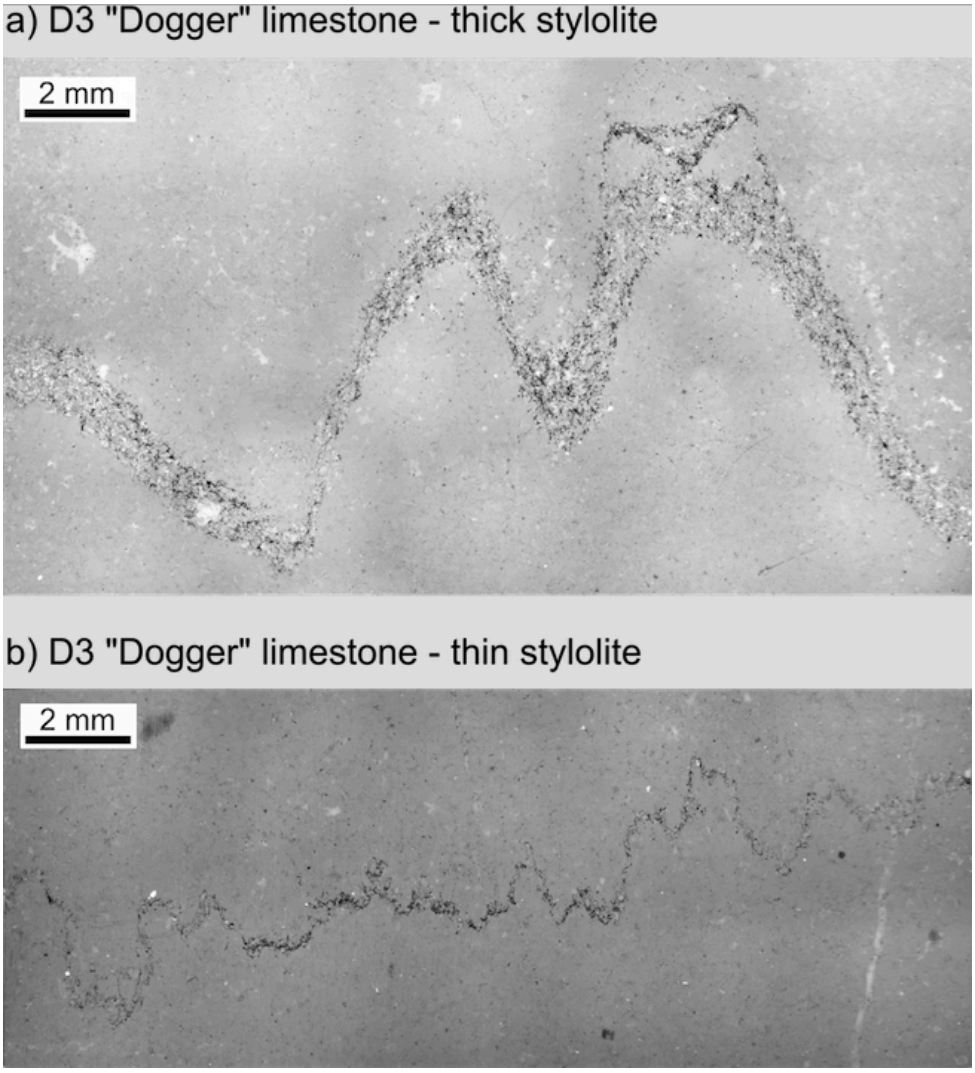

503

504

505 **Figure 4**. Optical microscope images of the stylolites found within studied limestones. (a) Corton

506 limestone from Burgundy. (b) Comblanchien limestone from Burgundy.

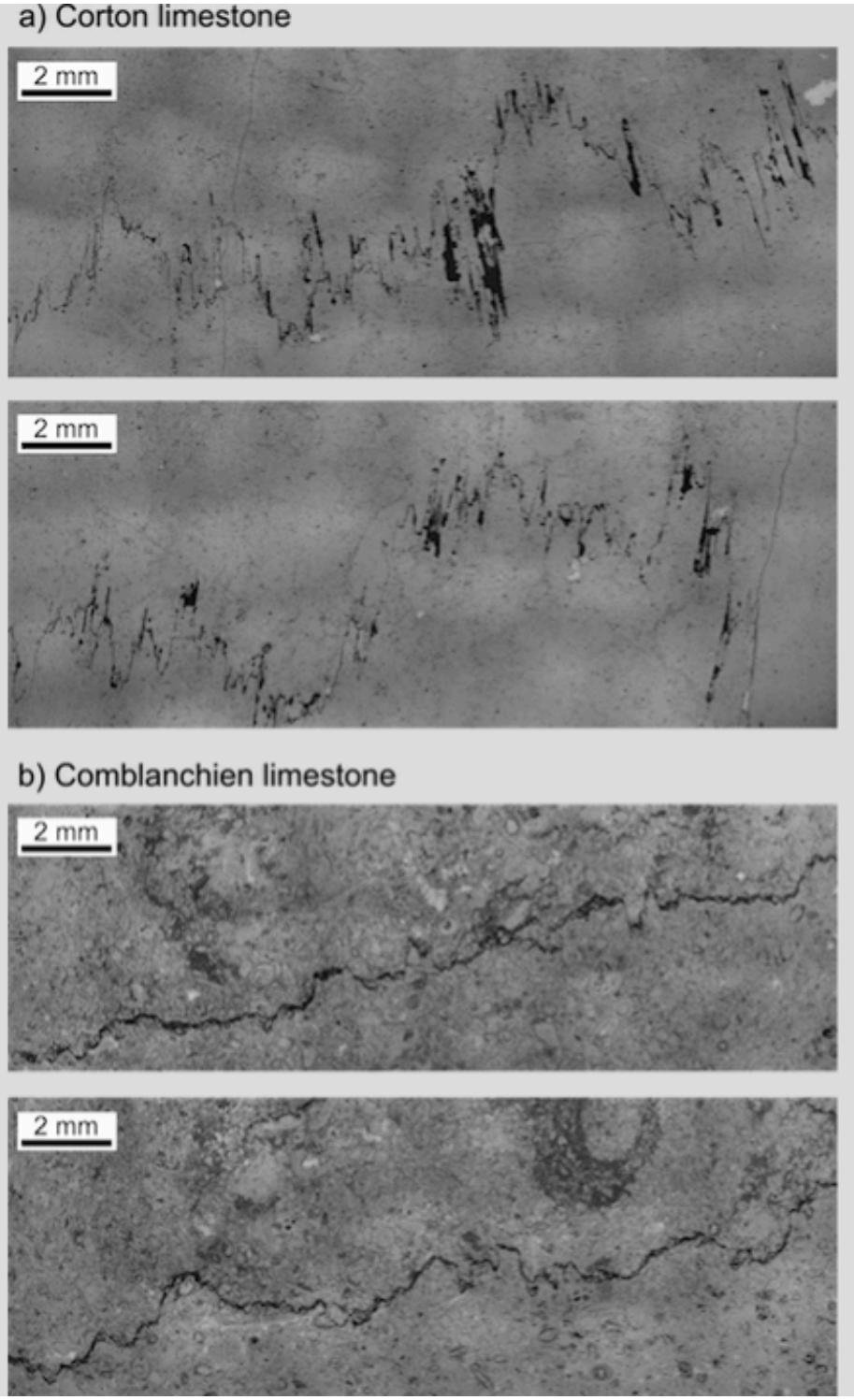

507

508 **Figure 5**. Optical microscope images of (a) a sedimentary stylolite and (b) a tectonic stylolite in

509 sample O3 – Oxfordian limestone from Bure.

510

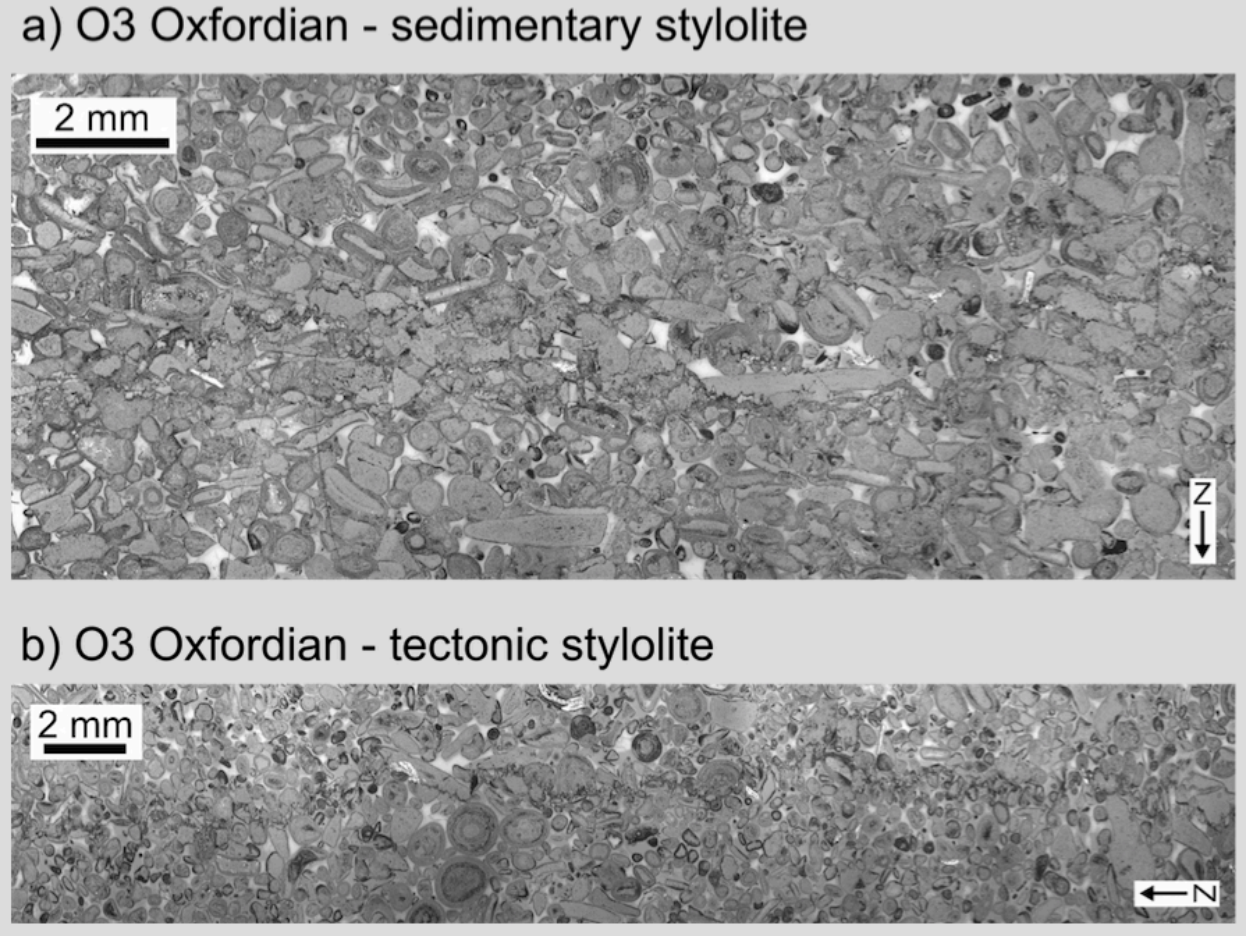

511

512

513

514 **Figure 6**. Photographs of the cylindrical samples prepared for laboratory measurements. Three
515 representative samples are shown for each lithology: an intact sample (on the left), a sample with a
516 stylolite perpendicular to flow (in the middle), and a sample with a stylolite parallel to flow (on the
517 right). (a) Sample O1 – Oxfordian limestone from Bure. (b) Sample O3 – Oxfordian limestone from
518 Bure. (c) Sample O6 – Oxfordian limestone from Bure. (d) Sample D3 – "Dogger" limestone from
519 Bure.

520

521 **Figure 7**. Photographs of the cylindrical samples prepared for laboratory measurements. Three
522 representative samples are shown for each lithology: an intact sample (on the left), a sample with a
523 stylolite perpendicular to flow (in the middle), and a sample with a stylolite parallel to flow (on the
524 right). (a) Corton limestone from Burgundy. (b) Comblanchien limestone from Burgundy.
525

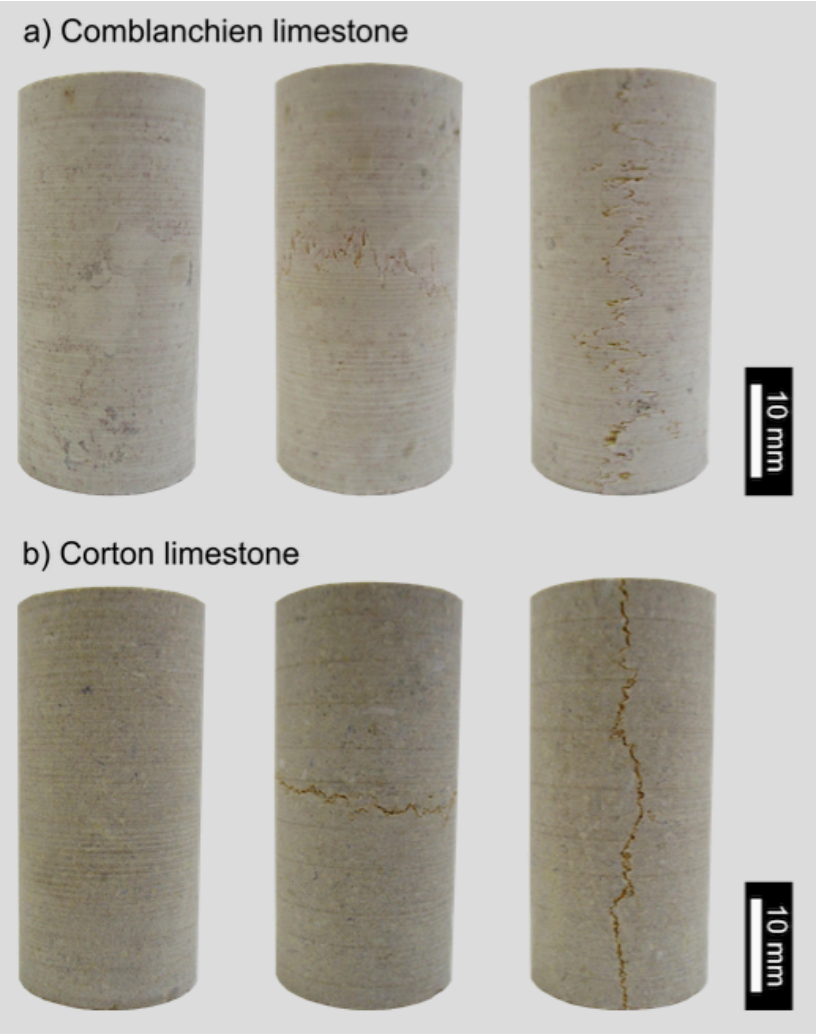

526
527

528 **Figure 8**. Photographs of the cylindrical samples containing either a tectonic stylolite (the two
529 samples on the left) or a sedimentary stylolite (the two samples on the right). All samples are from
530 sample O3 – Oxfordian limestone from Bure.
531

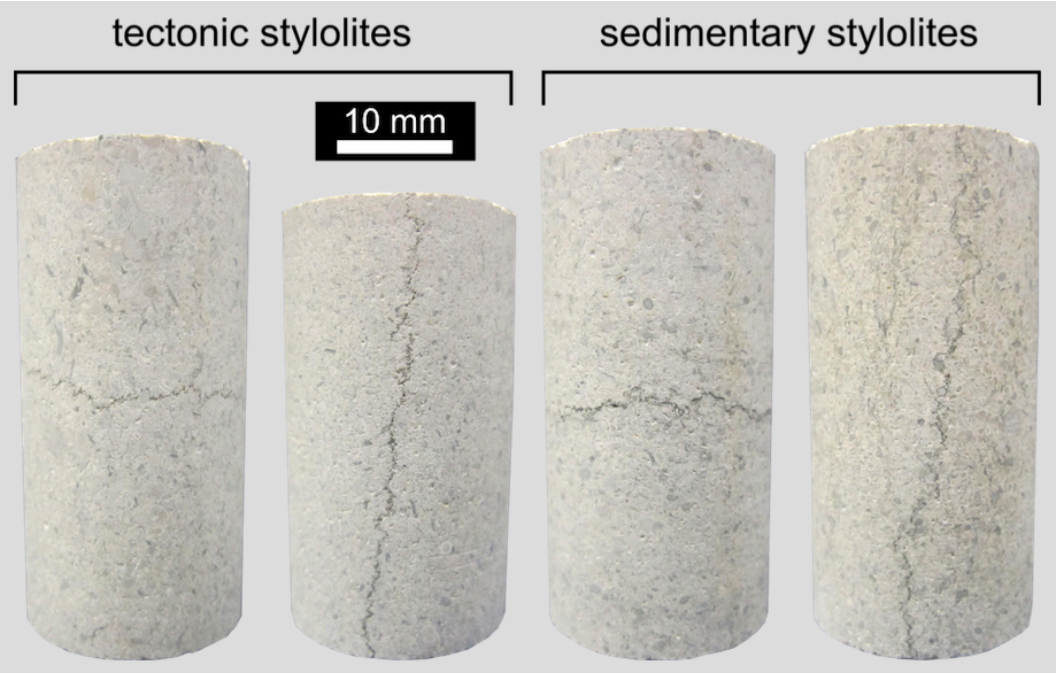

532
533
534

535 **Figure 9**. (a) Gas permeability (measured under a confining pressure of 2 MPa) as a function of
536 connected porosity for intact (i.e. stylolite-free) limestone. All datapoints above a porosity of 0.2 are
537 taken from Lind et al. (1994). (b) Gas permeability (measured under a confining pressure of 2 MPa)
538 as a function of connected porosity for limestone samples containing either a stylolite parallel to
539 flow or a stylolite perpendicular to flow. The gas permeabilities of the intact samples (i.e. the data of
540 panel (a)) are also plotted in panel (b).
541

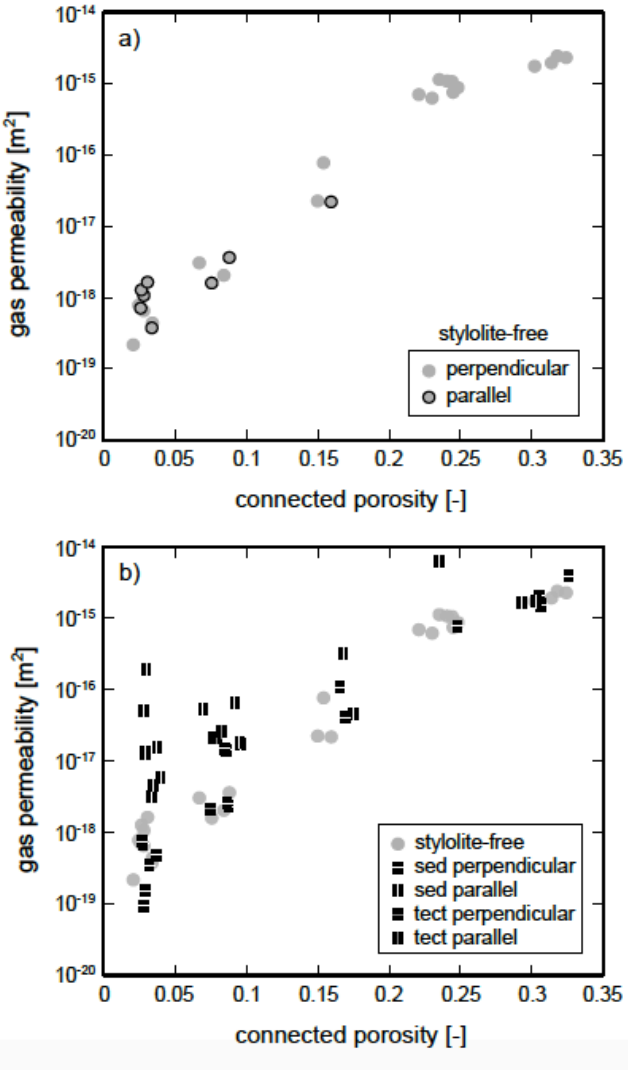

542
543

544 **Figure 10**. (a) The ratio of gas to water permeability as a function of connected porosity for intact
545 (i.e. stylolite-free) limestone. (b) The ratio of gas to water permeability as a function of connected
546 porosity for limestone samples containing either a stylolite parallel to flow or a stylolite
547 perpendicular to flow. The ratios of the intact samples (i.e. the data of panel (a)) are also plotted in
548 panel (b).
549

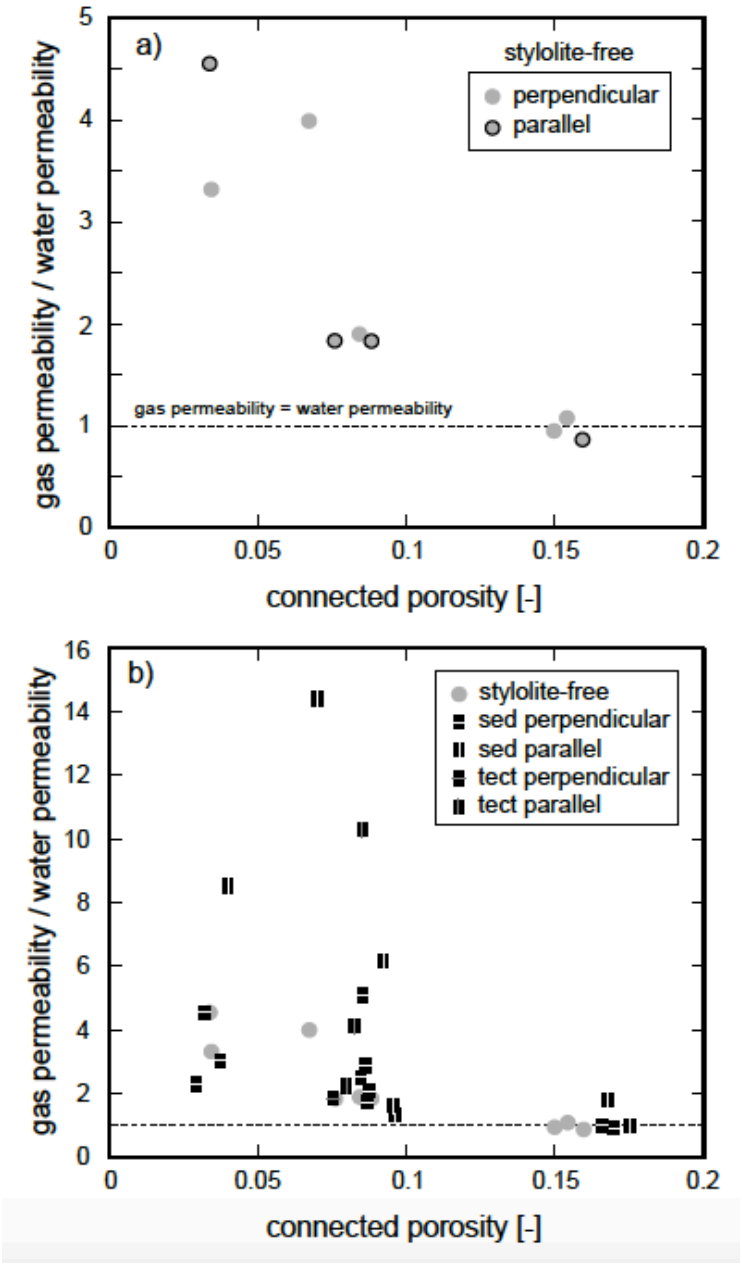

550

551 **Figure 11**. Backscattered scanning electron microscope image of the stylolite-host rock boundary
552 (sample D3 – "Dogger" limestone from Bure). Quartz grains within the stylolite are labelled. The
553 white arrows point to porosity (in black).
554

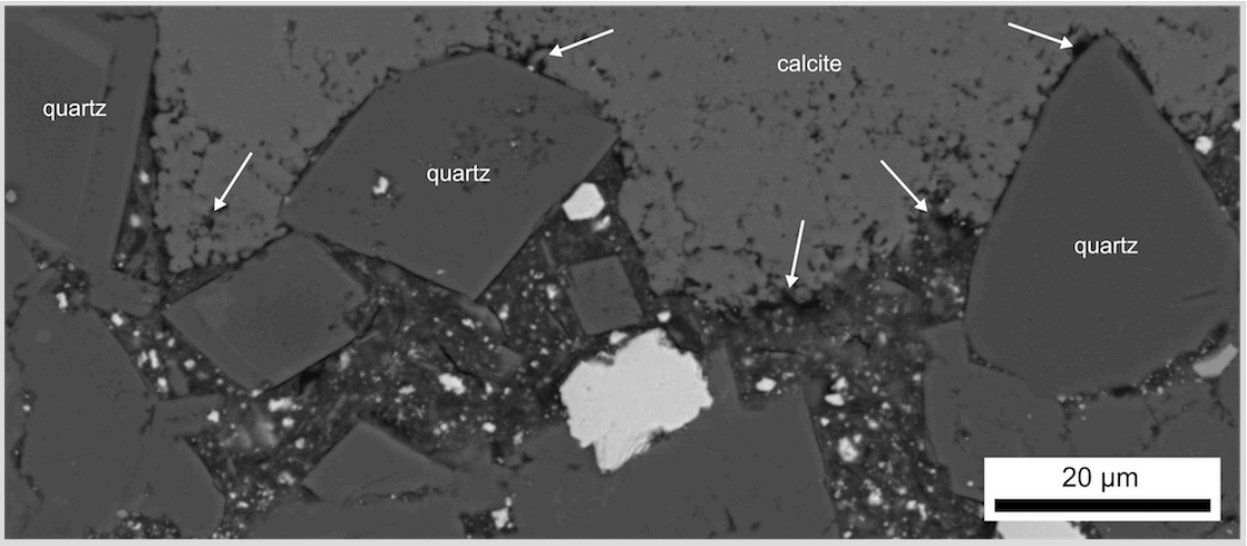

555
556
557

Figure 12. Multi-resolution X-ray synchrotron microtomography images of a stylolite in sample D3 ("Dogger" limestone from Bure). (a) An image of the stylolite at a voxel size of 6.27 µm. The coloured shapes are pores; individual pores are allocated different colours. (b) An image of the stylolite at a voxel size of 0.7 µm. The coloured shapes are pores; individual pores are allocated different colours.

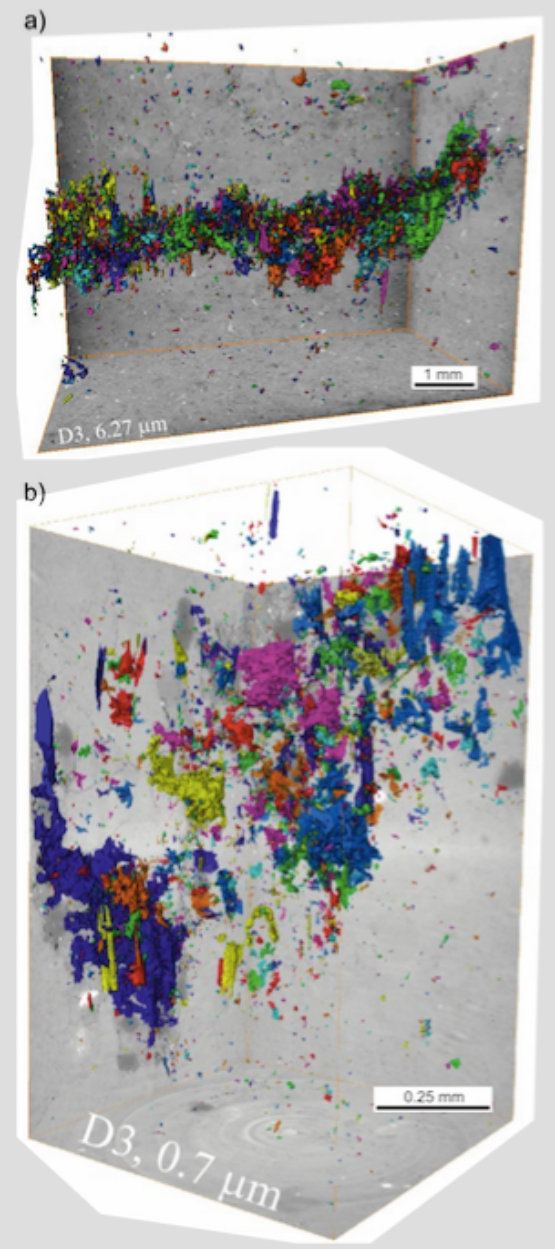

565 **Figure 13**. X-ray synchrotron microtomography image showing two pores within a stylolite in
566 sample D3 ("Dogger" limestone from Bure). The pores are "finger-like" in shape and are aligned
567 with the teeth of the stylolite.
568

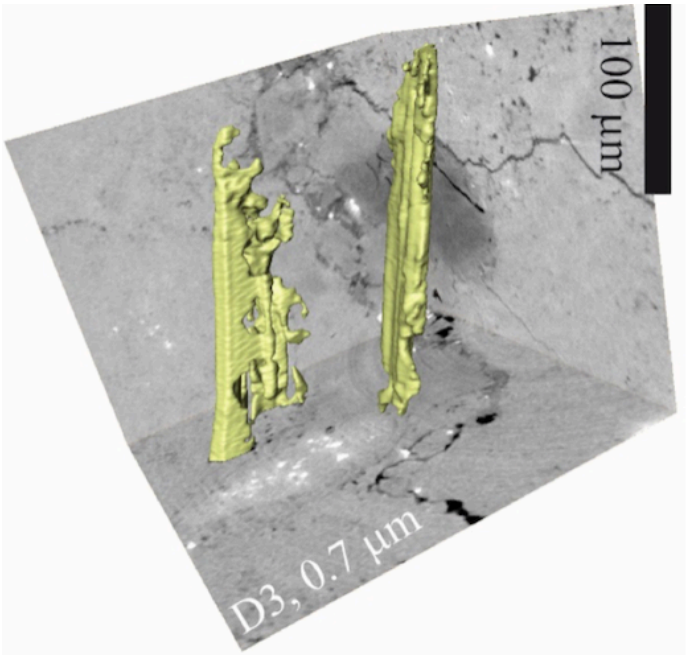

569
570
571

572 **Figure 14**. X-ray synchrotron microtomography data showing (a) the number of pores within a
573 subvolume of 0.16 mm^3 as a function of pore size inside and outside of a stylolite (sample D3 –
574 "Dogger" limestone from Bure) and (b) the probability density function as a function of sphericity
575 for the pores inside and outside of a stylolite (sample D3 – "Dogger" limestone from Bure). Two
576 subvolumes of sample D3 with the same volume of 0.16 mm^3, one inside the stylolite and one
577 outside of it, were used to perform these calculations.
578

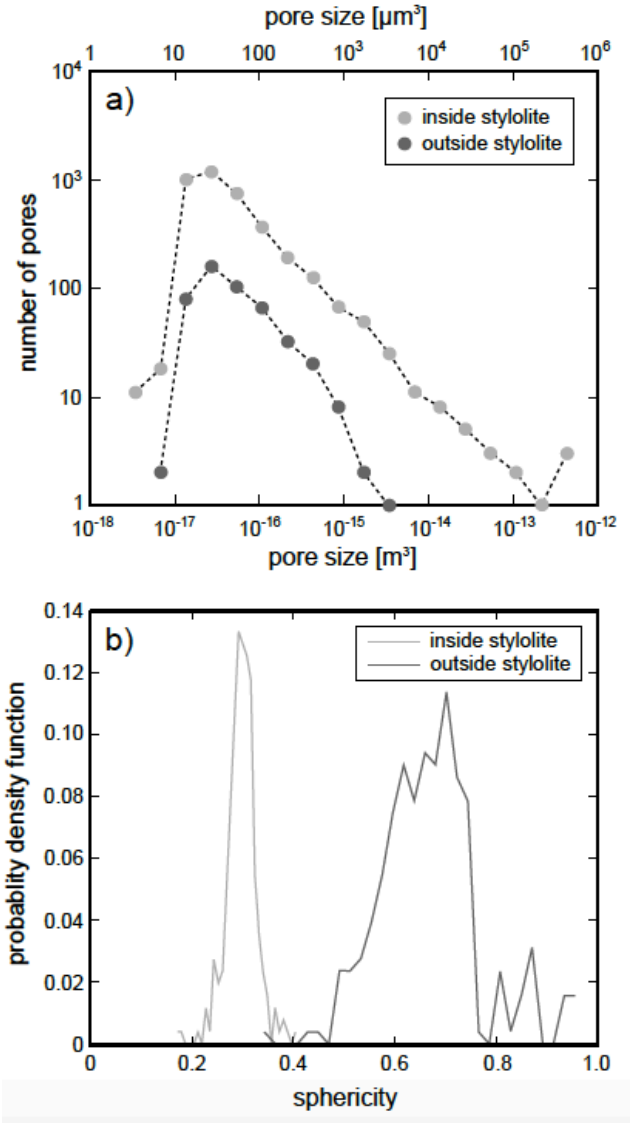

579
580

Figure 15. (a) The average pore radius of the flow path followed by the gas molecules (calculated using the Klinkenberg slip factor; see Equation 5) as a function of connected porosity for the intact (i.e. stylolite-free) samples. (a) The average pore radius of the pores used by the gas particles (calculated using the Klinkenberg slip factor; see Equation 5) as a function of connected porosity for limestone samples containing either a stylolite parallel to flow or a stylolite perpendicular to flow. The average pore radius of the intact samples (i.e. the data of panel (a)) are also plotted in panel (b).

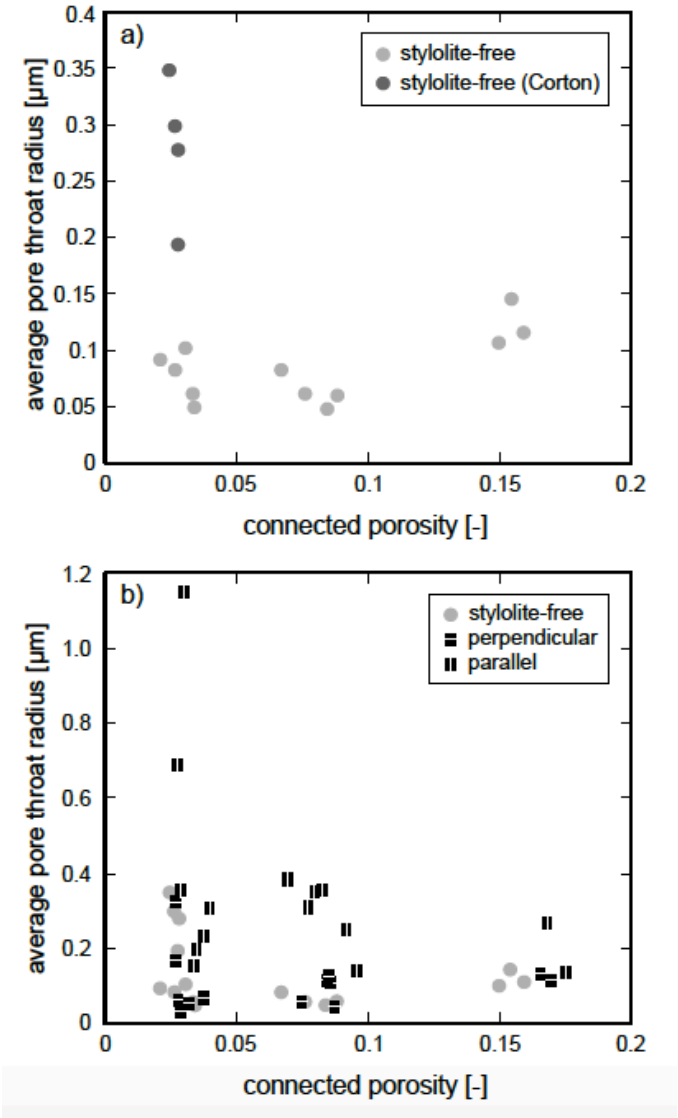

590 **Figure 16**. A photograph of a 78 mm-diameter core from Bure (sample D3 – "Dogger" limestone

591 from Bure). Arrows indicate the position of sedimentary stylolites.

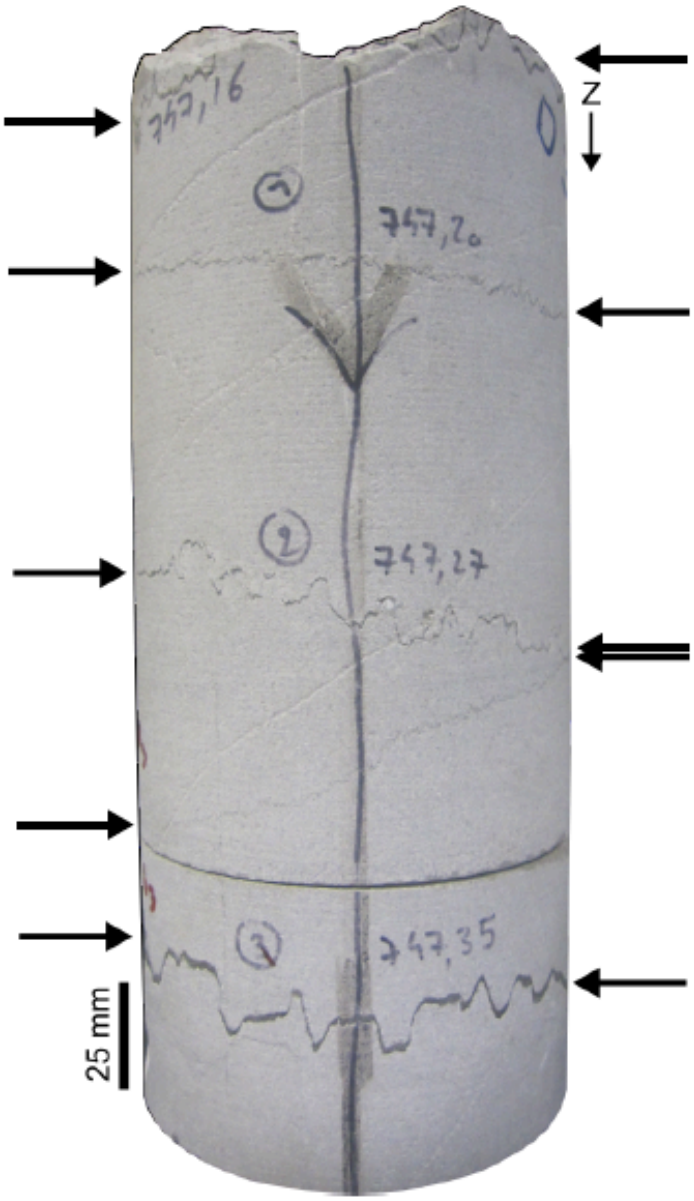

592

593 **Tables**

594

595 **Table 1**. X-ray powder diffraction (XRPD) analysis showing quantitative mineral composition for
596 the six limestones studied herein. Mineral contents of O1, O3, O6, and D3 were taken from Heap et
597 al. (2014).

Sample	**Stylolite-free composition (wt. %)**	**Minerals within the stylolite**
O1 (Oxfordian limestone)	99% calcite; <1% dolomite	dolomite, clay
O3 (Oxfordian limestone)	99% calcite, <1% dolomite; <1% gypsum; <<1% pyrite	dolomite, gypsum, pyrite, clay
O6 (Oxfordian limestone)	99% calcite, <1% dolomite; <<1% pyrite	dolomite, pyrite, clay
D3 ("Dogger" limestone)	93% quartz; 4% dolomite; 3% quartz; <<1% pyrite	dolomite, quartz, pyrite, clay
Corton limestone	99% calcite; <1% quartz	quartz, clay
Comblanchien limestone	99% calcite	clay

598

599

600 **Table 2**. Summary of the experimental data collected for this study. Porosities were measured
601 using the triple weight water saturation technique. Gas and water permeabilities were measured
602 under a confining pressure of 2 MPa. Gas permeabilities were measured with either argon or
603 nitrogen gas. Water permeabilities were measured with deionised water. Asterisk indicates that the
604 connected porosity and the gas permeability data were taken from Heap et al. (2014).

Sample	Description	Connected porosity	Gas permeability (m2)	Klinkenberg slip factor (MPa)	Water permeability (m2)	Gas/water permeability
*O1	No stylo perp	0.154	7.77×10^{-17}	0.189	7.22×10^{-17}	1.08
*O1	Sed stylo para	0.168	3.29×10^{-16}	0.102	1.81×10^{-16}	1.82
*O1	Sed stylo perp	0.166	1.09×10^{-16}	0.206	1.07×10^{-16}	1.02
*O3	No stylo perp	0.150	2.25×10^{-17}	0.309	2.37×10^{-17}	0.95
*O3	No stylo para	0.159	2.20×10^{-17}	0.286	2.54×10^{-17}	0.87
*O3	Sed stylo perp	0.169	4.10×10^{-17}	0.278	4.51×10^{-17}	0.91
*O3	Sed stylo para	0.175	4.65×10^{-17}	0.233	4.78×10^{-17}	0.97
O3	No stylo para	0.076	1.60×10^{-18}	0.449	8.72×10^{-19}	1.83
O3	No stylo para	0.088	3.63×10^{-18}	0.458	1.98×10^{-18}	1.83
O3	No stylo perp	0.084	2.05×10^{-18}	0.568	1.08×10^{-18}	1.90
O3	Tect stylo perp	0.075	2.14×10^{-18}	0.452	1.16×10^{-18}	1.84
O3	Tect stylo para	0.080	2.18×10^{-17}	0.079	9.73×10^{-18}	2.24
O3	Tect stylo para	0.082	2.62×10^{-17}	0.078	6.35×10^{-18}	4.13
O3	Tect stylo para	0.077	2.17×10^{-17}	0.089	7.17×10^{-18}	3.03
O3	Sed stylo perp	0.087	2.32×10^{-18}	0.621	1.12×10^{-18}	2.07
O3	Sed stylo perp	0.087	2.61×10^{-18}	0.537	1.51×10^{-18}	1.73
O3	Sed stylo para	0.096	1.75×10^{-17}	0.196	1.34×10^{-17}	1.31
O3	Sed stylo para	0.095	1.84×10^{-17}	0.195	1.15×10^{-17}	1.60
*O6	No stylo perp	0.067	3.04×10^{-18}	0.335	7.62×10^{-19}	3.99
*O6	Sed stylo para	0.070	5.36×10^{-17}	0.102	3.72×10^{-18}	14.41
*O6	Sed stylo para	0.092	6.58×10^{-17}	0.111	1.07×10^{-17}	6.15
*O6	Sed stylo	0.084	1.51×10^{-17}	0.241	6.04×10^{-18}	2.50

	perp					
*O6	Sed stylo perp	0.086	1.43×10^{-17}	0.252	4.98×10^{-18}	2.87
*O6	Sed stylo perp	0.085	1.39×10^{-17}	0.217	2.73×10^{-18}	5.09
*D3	No stylo perp	0.034	4.38×10^{-19}	0.557	1.32×10^{-19}	3.32
*D3	No stylo para	0.034	3.69×10^{-19}	0.447	8.11×10^{-20}	4.55
*D3	Sed stylo perp	0.037	4.88×10^{-19}	0.398	1.61×10^{-19}	3.03
*D3	Sed stylo perp	0.032	3.44×10^{-19}	0.521	7.55×10^{-20}	4.56
*D3	Sed stylo perp	0.029	1.56×10^{-19}	0.847	6.83×10^{-20}	2.28
*D3	Sed stylo para	0.040	5.98×10^{-18}	0.089	7.01×10^{-19}	8.53
COMB	No stylo para	0.031	1.64×10^{-18}	0.270	-	-
COMB	No stylo para	0.026	7.20×10^{-19}	0.335	-	-
COMB	Sed stylo para	0.037	1.54×10^{-17}	0.118	-	-
COMB	Sed stylo para	0.034	3.20×10^{-18}	0.180	-	-
COMB	Sed stylo para	0.035	4.64×10^{-18}	0.140	-	-
COMB	No stylo perp	0.021	2.18×10^{-19}	0.298	-	-
COMB	Sed stylo perp	0.027	6.95×10^{-19}	0.164	-	-
CORT	No stylo para	0.026	1.28×10^{-18}	0.092	-	-
CORT	No stylo para	0.028	1.07×10^{-18}	0.099	-	-
CORT	Sed stylo para	0.033	1.98×10^{-16}	0.024	-	-
CORT	Sed stylo para	0.030	5.22×10^{-17}	0.040	-	-
CORT	Sed stylo para	0.031	1.31×10^{-17}	0.078	-	-
CORT	No stylo perp	0.026	7.85×10^{-19}	0.079	-	-
CORT	No stylo perp	0.029	6.58×10^{-19}	0.142	-	-
CORT	Sed stylo perp	0.027	7.48×10^{-19}	0.085	-	-
CORT	Sed stylo perp	0.031	9.45×10^{-20}	0.433	-	-

605

606

607 **References**

608

609 Agosta, F., Ruano, P., Rustichelli, A., Tondi, E., Galindo-Zaldívar, J. and de Galdeano, C.S. 2012. Inner
610 structure and deformation mechanisms of normal faults in conglomerates and carbonate
611 grainstones (Granada Basin, Betic Cordillera, Spain): inferences on fault permeability. *Journal*
612 *of Structural Geology*, *45*, 4-20.
613 Alsharhan, A., and Sadd, J.L. 2000. Stylolites in Lower Cretaceous carbonate reservoirs, *U.A.E:*
614 *Society for Sedimentary Geology Special Publication*, *69*, 185–207.
615 Andrews, L.M. and Railsback, L.B. 1997. Controls on stylolite development: morphologic, lithologic,
616 and temporal evidence from bedding-parallel and transverse stylolites from the US
617 Appalachians. *The Journal of Geology*, *105*(1), 59-73.
618 Baud, P., Rolland, A., Heap, M., Xu, T., Nicolé, M., Ferrand, T., & Conil, N. 2016. Impact of stylolites on
619 the mechanical strength of limestone. *Tectonophysics*, *690*, 4-20.
620 Behnsen, J., & Faulkner, D. R. 2011. Water and argon permeability of phyllosilicate powders under
621 medium to high pressure. *Journal of Geophysical Research: Solid Earth*, *116*(B12), B12203,
622 doi:10.1029/2011JB008600
623 Benedicto, A., & Schultz, R. A. 2010. Stylolites in limestone: magnitude of contractional strain
624 accommodated and scaling relationships. *Journal of Structural Geology*, *32*(9), 1250-1256.
625 Bjørkum, P.A., Oelkers, E.H., Nadeau, P.H., Walderhaug, O. and Murphy, W.M. 1998. Porosity
626 prediction in quartzose sandstones as a function of time, temperature, depth, stylolite
627 frequency, and hydrocarbon saturation. *AAPG bulletin*, *82*(4), 637-648.
628 Braithwaite, C. J. R. 1989. Stylolites as open fluid conduits. *Marine and Petroleum Geology*, *6*(1), 93-
629 96.
630 Brouste, A., Renard, F., Gratier, J.P. and Schmittbuhl, J. 2007. Variety of stylolites' morphologies and
631 statistical characterization of the amount of heterogeneities in the rock. *Journal of Structural*
632 *Geology*, *29*(3), 422-434.
633 Burgess, C. J., & Peter, C. K. 1985. Formation, distribution, and prediction of stylolites as
634 permeability barriers in the Thamama Group, Abu Dhabi. In *Middle East Oil Technical*
635 *Conference and Exhibition*. Society of Petroleum Engineers.
636 Brace, W., Walsh, J. B., & Frangos, W. T. 1968. Permeability of granite under high pressure. *Journal of*
637 *Geophysical research*, *73*(6), 2225-2236.
638 Bruna, P. O., Lavenu, A. P., Matonti, C., & Bertotti, G. (2018). Are stylolites fluid-flow efficient
639 features? *Journal of Structural Geology*, doi: 10.1016/j.jsg.2018.05.018.
640 Carozzi, A. V., & Bergen, D. V. 1987. Stylolitic porosity in carbonates: a critical factor for deep
641 hydrocarbon production. *Journal of Petroleum Geology*, *10*(3), 267-282.
642 Civan, F. 2010. Effective correlation of apparent gas permeability in tight porous media. *Transport*
643 *in porous media*, *82*(2), 375-384.
644 Corwin, L. W., Broomhall, R. W., Saidikowski, R. M., & Wooten, J. N. (1997). Stylolites impact the
645 miscible nitrogen flood in a mature carbonate oil field. In: *Middle East Oil Show and*
646 *Conference*, Society of Petroleum Engineers, doi: doi.org/10.2118/37780-MS.
647 Croizé, D., Renard, F. and Gratier, J.P. 2013. Compaction and porosity reduction in carbonates: A
648 review of observations, theory, and experiments. *Advances in Geophysics*, *54*, 181-238.
649 Davy, C. A., Skoczylas, F., Barnichon, J. D., & Lebon, P. 2007. Permeability of macro-cracked argillite
650 under confinement: gas and water testing. *Physics and Chemistry of the Earth, Parts A/B/C*,
651 *32*(8-14), 667-680.
652 Dunnington, H. V. 1967. Aspects of diagenesis and shape change in stylolitic limestone reservoirs. In
653 *7th World Petroleum Congress*. World Petroleum Congress.

654 Dutton, S. P., & Willis, B. J. 1998. Comparison of outcrop and subsurface sandstone permeability
655 distribution, lower cretaceous fall river formation, South Dakota and Wyoming. *Journal of*
656 *Sedimentary Research*, *68*(5), 890-900.
657 Ebner, M., Koehn, D., Toussaint, R., Renard, F. and Schmittbuhl, J. 2009a. Stress sensitivity of
658 stylolite morphology. *Earth and Planetary Science Letters*, *277*(3), 394-398.
659 Ebner, M., Koehn, D., Toussaint, R. and Renard, F. 2009b. The influence of rock heterogeneity on the
660 scaling properties of simulated and natural stylolites. *Journal of Structural geology*, *31*(1), 72-
661 82.
662 Ebner, M., Piazolo, S., Renard, F. and Koehn, D. 2010a. Stylolite interfaces and surrounding matrix
663 material: Nature and role of heterogeneities in roughness and microstructural development.
664 *Journal of Structural Geology*, *32*(8), 1070-1084.
665 Ebner, M., Toussaint, R., Schmittbuhl, J., Koehn, D. and Bons, P. 2010b. Anisotropic scaling of
666 tectonic stylolites: A fossilized signature of the stress field?. *Journal of Geophysical Research:*
667 *Solid Earth*, *115*(B6), B06403, doi:10.1029/2009JB006649.
668 Emmanuel, S., Ague, J. J., & Walderhaug, O. (2010). Interfacial energy effects and the evolution of
669 pore size distributions during quartz precipitation in sandstone. *Geochimica et Cosmochimica*
670 *Acta*, *74*(12), 3539-3552.
671 Fabricius, I.L. and Borre, M.K. 2007. Stylolites, porosity, depositional texture, and silicates in chalk
672 facies sediments. Ontong Java Plateau–Gorm and Tyra fields, North Sea. *Sedimentology*, *54*(1),
673 183-205.
674 Farquharson, J. I., Heap, M. J., Lavallée, Y., Varley, N. R., & Baud, P. 2016. Evidence for the
675 development of permeability anisotropy in lava domes and volcanic conduits. *Journal of*
676 *Volcanology and Geothermal Research*, *323*, 163-185.
677 Faulkner, D. R., & Rutter, E. H. 2000. Comparisons of water and argon permeability in natural clay-
678 bearing fault gouge under high pressure at 20° C. *Journal of Geophysical Research: Solid Earth*,
679 *105*(B7), 16415-16426.
680 Faulkner, D. R., & Rutter, E. H. 2003. The effect of temperature, the nature of the pore fluid, and
681 subyield differential stress on the permeability of phyllosilicate-rich fault gouge. *Journal of*
682 *Geophysical Research: Solid Earth*, *108*(B5), 2227, doi:10.1029/2001JB001581.
683 Finkel, E. A., & Wilkinson, B. H. 1990. Stylolitization as Source of Cement in Mississippian Salem
684 Limestone, West-Central Indiana (1). *AAPG Bulletin*, *74*(2), 174-186.
685 Firouzi, M., Alnoaimi, K., Kovscek, A., & Wilcox, J. 2014. Klinkenberg effect on predicting and
686 measuring helium permeability in gas shales. *International Journal of Coal Geology*, *123*, 62-
687 68.
688 Forchheimer, P. (1901). Wasserbewegung durch boden. *Z. Ver. Deutsch, Ing.*, *45*, 1782-1788.
689 Ford, D., & Williams, P. D. 2013. *Karst Hydrogeology and Geomorphology*. John Wiley & Sons.
690 Gingras, M. K., MaCmillan, B., & Balcom, B. J. 2002. Visualizing the internal physical characteristics of
691 carbonate sediments with magnetic resonance imaging and petrography. *Bulletin of Canadian*
692 *Petroleum Geology*, *50*(3), 363-369.
693 Heald, M.T., 1955. Stylolites in sandstones. *The Journal of Geology*, *63*(2), 101-114.
694 Heap, M.J., Baud, P., Reuschlé, T. and Meredith, P.G. 2014. Stylolites in limestones: Barriers to fluid
695 flow?. *Geology*, *42*(1), 51-54.
696 Heap, M. J., & Kennedy, B. M. 2016. Exploring the scale-dependent permeability of fractured
697 andesite. *Earth and Planetary Science Letters*, *447*, 139-150.
698 Heap, M. J., Kushnir, A. R., Gilg, H. A., Wadsworth, F. B., Reuschlé, T., & Baud, P. 2017. Microstructural
699 and petrophysical properties of the Permo-Triassic sandstones (Buntsandstein) from the
700 Soultz-sous-Forêts geothermal site (France). *Geothermal Energy*, *5*(1), 26.
701 Heap, M. J., Reuschlé, T., Farquharson, J. I., & Baud, P. 2018. Permeability of volcanic rocks to gas and
702 water. *Journal of Volcanology and Geothermal Research*, *354*, 29-38.

Heller, R., Vermylen, J., & Zoback, M. 2014. Experimental investigation of matrix permeability of gas shales. *AAPG Bulletin*, *98*(5), 975-995.

Iezzi, G., Ventura, G. D., Oberti, R., Cámara, F., & Holtz, F. 2004. Synthesis and crystal-chemistry of Na (NaMg) Mg5Si8O22 (OH) 2, a P 21/m amphibole. *American Mineralogist*, *89*(4), 640-646.

Iezzi, G., Della Ventura, G., Tribaudino, M., Nemeth, P., Margiolaki, I., Cavallo, A.,. & Behrens, H. 2010. Phase transition induced by solid solution: The ^{B}Ca-^{B}Mg substitution in richteritic amphiboles. *American Mineralogist*, *95*(2-3), 369-381.

Ji, Y., Baud, P., Vajdova, V., & Wong, T.-f. 2012. Characterization of pore geometry of Indiana limestone in relation to mechanical compaction. *Oil & Gas Science and Technology–Revue d'IFP Energies Nouvelles*, *67*(5), 753-775.

Ji, Y., Hall, S. A., Baud, P., & Wong, T.-f. 2014. Characterization of pore structure and strain localization in Majella limestone by X-ray computed tomography and digital image correlation. *Geophysical Journal International*, *200*(2), 701-719.

Karcz, Z. and Scholz, C.H. 2003. The fractal geometry of some stylolites from the Calcare Massiccio Formation, Italy. *Journal of Structural Geology*, *25*(8), 1301-1316.

Klinkenberg, L. J. (1941). The permeability of porous media to liquids and gases. In *Drilling and production practice*. American Petroleum Institute.

Koehn, D., Renard, F., Toussaint, R. and Passchier, C.W. 2007. Growth of stylolite teeth patterns depending on normal stress and finite compaction. *Earth and Planetary Science Letters*, *257*(3), 582-595.

Koehn, D., Ebner, M., Renard, F., Toussaint, R. and Passchier, C.W. 2012. Modelling of stylolite geometries and stress scaling. *Earth and Planetary Science Letters*, *341*, 104-113.

Koehn, D., Rood, M. P., Beaudoin, N., Chung, P., Bons, P. D., & Gomez-Rivas, E. 2016. A new stylolite classification scheme to estimate compaction and local permeability variations. *Sedimentary Geology*, *346*, 60-71.

Koepnick, R. B. 1987. Distribution and permeability of stylolite-bearing horizons within a Lower Cretaceous carbonate reservoir in the Middle East. *SPE Formation Evaluation*, *2*(02), 137-142.

Kushnir, A. R., Heap, M. J., & Baud, P. 2018. Assessing the role of fractures on the permeability of the Permo-Triassic sandstones at the Soultz-sous-Forêts (France) geothermal site. *Geothermics*, *74*, 181-189.

Laronne Ben-Itzhak, L.L., Aharonov, E., Toussaint, R. and Sagy, A. 2012. Upper bound on stylolite roughness as indicator for amount of dissolution. *Earth and Planetary Science Letters*, *337*, 186-196.

Laronne Ben-Itzhak, L.L., Aharonov, E., Karcz, Z., Kaduri, M. and Toussaint, R. 2014. Sedimentary stylolite networks and connectivity in Limestone: Large-scale field observations and implications for structure evolution. *Journal of Structural Geology*, *63*, 106-123.

Larson, A. C., & Von Dreele, R. B. 1994. GSAS. *Report lAUR*, 86-748.

Letham, E. A., & Bustin, R. M. 2016. The impact of gas slippage on permeability effective stress laws: Implications for predicting permeability of fine-grained lithologies. *International Journal of Coal Geology*, *167*, 93-102.

Lind, I., Nykjaer, O., Priisholm, S. and Springer, N. 1994. Permeability of stylolite-bearing chalk. *Journal of Petroleum Technology*, *46*(11), 986-993.

Mallon, A.J. and Swarbrick, R.E. 2008. Diagenetic characteristics of low permeability, non-reservoir chalks from the Central North Sea. *Marine and Petroleum Geology*, *25*(10), 1097-1108.

Martín-Martín, J. D., Gomez-Rivas, E., Gómez-Gras, D., Travé, A., Ameneiro, R., Koehn, D., & Bons, P. D. 2018. Activation of stylolites as conduits for overpressured fluid flow in dolomitized platform carbonates. *Geological Society, London, Special Publications*, *459*(1), 157-176.

Nelson, R. A. 1981. Significance of fracture sets associated with stylolite zones: geologic notes. *AAPG Bulletin*, *65*(11), 2417-2425.

752 Nenna, F. and Aydin, A. 2011. The formation and growth of pressure solution seams in clastic rocks:
753 A field and analytical study. *Journal of Structural Geology*, *33*(4), 633-643.
754 Padmanabhan, E., Sivapriya, B., Huang, K. H., Askury, A. K., & Chow, W. S. 2015. The impact of
755 stylolites and fractures in defining critical petrophysical and geomechanical properties of
756 some carbonate rocks. *Geomechanics and Geophysics for Geo-Energy and Geo-Resources*, *1*(1-
757 2), 55-67.
758 Park, W.C. and Schot, E.H. 1968. Stylolites: their nature and origin. *Journal of Sedimentary Research*,
759 *38*(1), 175-191.
760 Railsback, L.B. and Andrews, L.M. 1995. Tectonic stylolites in the 'undeformed' Cumberland Plateau
761 of southern Tennessee. *Journal of Structural Geology*, *17*(6), 911-915.
762 Raynaud, S., & Carrio-Schaffhauser, E. 1992. Rock matrix structures in a zone influenced by a
763 stylolite. *Journal of Structural Geology*, *14*(8-9), 973-980.
764 Renard, F., Schmittbuhl, J., Gratier, J.P., Meakin, P. and Merino, E. 2004. Three-dimensional
765 roughness of stylolites in limestones. *Journal of Geophysical Research: Solid Earth*, *109*(B3),
766 B03209, doi:10.1029/2003JB002555.
767 Rolland, A., Toussaint, R., Baud, P., Schmittbuhl, J., Conil, N., Koehn, D., Renard, F. and Gratier, J.P.
768 2012. Modeling the growth of stylolites in sedimentary rocks. *Journal of Geophysical Research:*
769 *Solid Earth*, *117*(B6), B06403, doi:10.1029/2011JB009065.
770 Rolland, A., Toussaint, R., Baud, P., Conil, N., & Landrein, P. 2014. Morphological analysis of stylolites
771 for paleostress estimation in limestones. *International Journal of Rock Mechanics and Mining*
772 *Sciences*, *67*, 212-225.
773 Rustichelli, A., Tondi, E., Agosta, F., Cilona, A. and Giorgioni, M. 2012. Development and distribution
774 of bed-parallel compaction bands and pressure solution seams in carbonates (Bolognano
775 Formation, Majella Mountain, Italy). *Journal of Structural Geology*, *37*, 181-199.
776 Rustichelli, A., Tondi, E., Korneva, I., Baud, P., Vinciguerra, S., Agosta, F., Reuschlé, T. and Janiseck,
777 J.M. 2015. Bedding-parallel stylolites in shallow-water limestone successions of the Apulian
778 Carbonate Platform (central-southern Italy). *Italian Journal of Geosciences*, *134*(3), 513-534.
779 Scheidegger, A. E. 1974. *The Physics of Flow through Porous Media* (No. 532.5 S2 1974).
780 Schmittbuhl, J., Renard, F., Gratier, J.P. and Toussaint, R. 2004. Roughness of stylolites: implications
781 of 3D high resolution topography measurements. *Physical Review Letters*, *93*(23), p.238501.
782 Smith, S. A., Billi, A., Di Toro, G., & Spiess, R. 2011. Principal slip zones in limestone: microstructural
783 characterization and implications for the seismic cycle (Tre Monti Fault, Central Apennines,
784 Italy). *Pure and Applied Geophysics*, *168*(12), 2365-2393.
785 Tanikawa, W., & Shimamoto, T. 2006. Klinkenberg effect for gas permeability and its comparison to
786 water permeability for porous sedimentary rocks. *Hydrology and Earth System Sciences*
787 *Discussions*, *3*(4), 1315-1338.
788 Tanikawa, W., & Shimamoto, T. 2009. Comparison of Klinkenberg-corrected gas permeability and
789 water permeability in sedimentary rocks. *International Journal of Rock Mechanics and Mining*
790 *Sciences*, *46*(2), 229-238.
791 Toby, B. H. 2001. EXPGUI, a graphical user interface for GSAS. *Journal of Applied Crystallography*,
792 *34*(2), 210-213.
793 Tondi, E., Antonellini, M., Aydin, A., Marchegiani, L. and Cello, G. 2006. The role of deformation
794 bands, stylolites and sheared stylolites in fault development in carbonate grainstones of
795 Majella Mountain, Italy. *Journal of Structural Geology*, *28*(3), 376-391.
796 Toussaint, R., Aharonov, E., Koehn, D., Gratier, J. P., Ebner, M., Baud, P., ... & Renard, F. (2018).
797 Stylolites: A review. *Journal of Structural Geology*, *114*, 163-195.
798 Vajdova, V., Baud, P., & Wong, T. F. 2004. Permeability evolution during localized deformation in
799 Bentheim sandstone. *Journal of Geophysical Research: Solid Earth*, *109*(B10), B10406,
800 doi:10.1029/2003JB002942.

Van Geet, M., Swennen, R., & Wevers, M. 2000. Quantitative analysis of reservoir rocks by microfocus X-ray computerised tomography. *Sedimentary Geology*, *132*(1-2), 25-36.
Walderhaug, O. 1996. Kinetic modeling of quartz cementation and porosity loss in deeply buried sandstone reservoirs. *AAPG bulletin*, *80*(5), 731-745.
Walderhaug, O., & Bjørkum, P. A. (2003). The effect of stylolite spacing on quartz cementation in the Lower Jurassic Stø Formation, southern Barents Sea. *Journal of Sedimentary Research*, *73*(2), 146-156.
Wanless, H.R. 1979. Limestone response to stress: pressure solution and dolomitization. *Journal of Sedimentary Research*, *49*(2), 437-462.
Zinszner, B., & Pellerin, F. M. 2007. *A Geoscientist's Guide to Petrophysics*. Editions Technip. ISBN: 9782710808992.